


## Effect of catalyst support on dihydroeugenol hydrodeoxygenation on low cost FeNi catalyst to produce renewable alkane fuel

Zuzana Vajglová<sup>a</sup>, Päivi Mäki-Arvela<sup>a</sup>, Olha Yevdokimova<sup>a</sup>, Mark Martinez-Klimov<sup>a</sup>, Irina Simakova<sup>a</sup>, Kari Eränen<sup>a</sup>, Teija Tirri<sup>a</sup>, Jessi E.S. van Hoeven<sup>b</sup>, Anssi Peuronen<sup>c</sup>, Matej Huš<sup>d,e</sup>, Blaž Likozar<sup>d</sup>, Mika Lastusaari<sup>c</sup>, Johan Lindén<sup>a</sup>, Dmitry E. Doronkin<sup>f</sup>, Dmitry Yu. Murzin<sup>a,\*</sup> 

<sup>a</sup> Laboratory of Industrial Chemistry and Reaction Engineering, Åbo Akademi University, Turku, Finland

<sup>b</sup> Materials Chemistry and Catalysis, Debye Institute for Nanomaterials Science, Utrecht University, Universiteitsweg 99, Utrecht 3584 CG, the Netherlands

<sup>c</sup> Department of Chemistry, University Turku, Turku, Finland

<sup>d</sup> National Institute of Chemistry, Ljubljana, Slovenia

<sup>e</sup> Association for Technical Culture of Slovenia (ZOTKS), Ljubljana, Slovenia

<sup>f</sup> Karlsruhe Institute of Technology, Karlsruhe, Germany

### ARTICLE INFO

#### Keywords:

Hydrodeoxygenation

Dihydroeugenol

Fe-Ni catalysts

### ABSTRACT

Solventless hydrodeoxygenation of dihydroeugenol was investigated in a continuous reactor at 300 °C under 30 bar over different nickel-iron catalysts, prepared using a two-step impregnation method. The following catalysts were studied: mesoporous FeNi/Al<sub>2</sub>O<sub>3</sub>, FeNi/SiO<sub>2</sub> and FeNi/H-MCM-48 as well as microporous FeNi/H-Beta-300, FeNi/H-Beta-38, FeNi/H-Y-5.1, FeNi/H-MCM-48 and FeNi/USY-30. The catalysts were characterized by SEM coupled with energy dispersive X-ray analysis, Mössbauer and X-ray absorption spectroscopy, hydrogen TPR, X-ray diffraction, TEM, nitrogen physisorption and FTIR pyridine adsorption. DFT calculations were performed to elucidate the role of Fe and Ni. The results revealed that FeNi/Al<sub>2</sub>O<sub>3</sub> was the most active and stable in dihydroeugenol hydrodeoxygenation. Complete conversion of dihydroeugenol was obtained and the yield of the main product propylcyclohexane was varying in the range 84–88 %. FeNi/Al<sub>2</sub>O<sub>3</sub> catalyst exhibited 3.4 nm metal particles and contained FeNi alloy particles with the fcc metallic structure. No deactivation was observed for FeNi/Al<sub>2</sub>O<sub>3</sub> during 5 hours time-on-stream due to the presence of Ni-rich particles with iron-enriched outer surface confirmed by EXAFS. Fe was shown to be responsible for deoxygenation, while Ni promotes hydrogenation. Catalyst deactivation was observed for all other catalysts except for FeNi/Al<sub>2</sub>O<sub>3</sub> with increasing time-on-stream under the same reaction conditions due to their higher Brønsted to Lewis acid site ratio and larger average metal particle size in comparison to FeNi/Al<sub>2</sub>O<sub>3</sub>.

### 1. Introduction

Fuels from renewable sources are of great interest as they can be a solution to several economic and environmental problems [1]. Biomass is obtained from biowaste, wood, various parts of plants and even animal origin and is a green source of bio-oils [2]. Bio-oils as such cannot be used as fuels directly because of many reasons. The most important of them are their high oxygen content and low stability. The most common way to improve the quality of bio-oils is hydrodeoxygenation (HDO) process which removes oxygen from oxygen-containing compounds. Moreover, this is the cheapest way to get deoxygenated hydrocarbon

fuels directly from bio-oils [3].

In kinetic studies model compounds, which are found in bio-oils, are typically used. As a model compound in this work dihydroeugenol was applied, as it has hydroxyl, methoxy- and allyl groups which are the representative ones for bio-oils derived from lignin [3,4]. Isoeugenol HDO has been intensively studied both over noble metal [5,6] and non-noble transition metal catalysts [7,8].

While several noble metal catalysts like Pt, Ir have been used for HDO of bio-oils [3–6,9,10], there is a need in finding a cheaper way for bio-oils reforming. In [11–13], it was already confirmed that supported non-noble metals are promising catalysts for HDO of lignin derived

\* Corresponding author.

E-mail address: [dmurzin@abo.fi](mailto:dmurzin@abo.fi) (D.Yu. Murzin).

<https://doi.org/10.1016/j.apcata.2025.120307>

Received 3 March 2025; Received in revised form 7 April 2025; Accepted 21 April 2025

Available online 23 April 2025

0926-860X/© 2025 The Author(s). Published by Elsevier B.V. This is an open access article under the CC BY license (<http://creativecommons.org/licenses/by/4.0/>).

model compounds in a batch mode. The deoxygenation degree depends also on conditions and the reactant. For example, in vanillin hydrodeoxygenation at 130 °C under 10 bar hydrogen, nickel based mixed metal oxide (MMO) catalyst,  $\text{Ni}_{0.5}\text{Zn}_{1.5}\text{Al}_1\text{-MMO}$ , was active, however, giving only a partial oxygen removal [14]. Limited information about HDO of lignin derived model compounds can be found in a continuous mode and, moreover, such reactions were performed mainly in the gas phase [15].

Not only the metal nature can affect the reaction rate, conversion, and selectivity but also the support material type. Support acidity and the pore structure are the most important parameters that can have an influence the reaction [16]. Zeolites are often used catalysts for bio-oil transformations due to their morphology and a controlled ratio of aluminium and silicon influencing acidity [17]. Namely, H-Beta-38 has more acid sites than H-Beta-300, which showed to be beneficial for removal of oxygen. On the contrary, too high acidity of the catalyst could lead to the undesired reactions, such as alkylation [18,19] and potentially coking. For instance,  $\text{Al}_2\text{O}_3$  as a support has only Lewis acid sites that are more active in HDO reactions than the Brønsted acid sites, which was demonstrated in [20–22]. At the same time  $\text{SiO}_2$  support is more stable than alumina, however, bearing no acidity [23]. On the other hand, H-USY-30 has rather large pores and high stability [23]. Recently, new types of materials have been synthesized and tested in various reactions, such as MCM-48, which is a type of highly ordered mesoporous aluminosilicate with acidic properties [24]. Al-MCM-48 has also been successfully used in several reactions, such as hydrolytic hydrogenation of hemicellulose and production of furfural transformation from levoglucosan [25,26].

The aim of this work is to compare the effect of the catalyst support, its porosity and acidity and to find the best support for bimetallic non-noble Fe/Ni catalysts for HDO of dihydroeugenol (Fig. 1) in a continuous mode.

The novelty of this work is in elucidation of the role of Fe and Ni in the catalyst and proposing the reaction mechanism based on detailed catalyst characterization, reactivity studies and theoretical insight.

In the previous work of our group [27] continuous HDO of isoeugenol and dihydroeugenol was investigated in a fixed bed reactor using FeNi/H-Beta-300 as a catalyst. After obtaining promising results, it was decided to investigate also the effect of the support in HDO of dihydroeugenol, which is the aim of the current work. The following supports were used for preparation, characterisation and testing in HDO of dihydroeugenol: zeolites H-USY-30, H-Y-5.1, H-Beta-38, H-Beta-300 and mesoporous H-Al-MCM-48 as well as  $\text{SiO}_2$ ,  $\text{Al}_2\text{O}_3$ . A comprehensive catalyst characterization was performed including nitrogen adsorption,

transmission and scanning electron microscopy, energy dispersive X-ray analysis, temperature programmed reduction, pyridine adsorption desorption, Mössbauer spectroscopy, X-ray diffraction and X-ray absorption spectroscopy. A special emphasis was put on determination of the local environment of metals and the possible presence of alloys. In addition, the spent catalysts were characterized by thermogravimetric analysis to determine the amount of formed coke. The ultimate aim was to correlate performance of the catalysts with their properties and to reveal the reaction mechanism.

## 2. Experimental

### 2.1. Catalyst preparation method

The following materials were used as supports: H-Y-5.1,  $\text{NH}_4\text{-Beta-38}$ , H-Beta-300 were purchased from Zeolyst International,  $\text{SiO}_2$  from Sigma Aldrich and  $\text{Al}_2\text{O}_3$  from UOP LCC, while H-Al-MCM-48 was synthesized according to [26], H-USY-30 was prepared according to the procedure reported in [28]. As iron and nickel sources the following precursors were used:  $\text{Fe}(\text{NO}_3)_3 \cdot 9 \text{H}_2\text{O}$  (Sigma-Aldrich),  $\text{Ni}(\text{NO}_3)_2 \cdot 6 \text{H}_2\text{O}$  (CJSC Souzchimprom).

The commercial  $\text{NH}_4\text{-Beta-38}$  was transformed to H-Beta-38 protonic form by heating to 250 °C with a temperature ramp 4 °C/min (60 min), and thereafter to 500 °C with a temperature ramp 2 °C/min for 4 h [29].

The H-Beta-300 sample was calcined prior to the metal loading using the following temperature programme: 4 °C/min-250 °C (50 min)-2 °C/min -500 °C (4 h). Other zeolite and metal oxide support materials were dried at 100 °C for 17 h before metal loading.

The supported FeNi catalysts with metal loading 5 wt% Fe and 5 wt % Ni were prepared by the two-step subsequent impregnation method. First the support was impregnated with an iron nitrate aqueous solution (1.6 M) following by drying at 100 °C for 10 h. Then, the nickel nitrate aqueous solution (1.5 M) was introduced into Fe containing support followed by drying at 100 °C for 10 h and calcination in air at 450 °C (temperature ramp 2 °C/min) for 6 h.

All prepared FeNi catalysts were activated in hydrogen flow at 500 °C before the reaction (see Section 2.3 Experimental setup).

### 2.2. Catalyst characterization methods

Textural properties were determined by nitrogen adsorption using Micromeritics 3Flex-3500 J followed by in situ evacuation for 3 h at 250 °C. For determination of the surface area either Dubinin-Radushkevich or BET methods were applied for microporous and mesoporous materials, respectively, while the pore size distribution was calculated using the non-local density functional (DFT) method.

TEM measurements were performed with a Jeol JEM 1400 Plus instrument and the metal particle sizes were determined with Fiji ImageJ software.

Scanning Transmission Electron Microscopy (STEM) images and energy dispersive X-ray spectroscopy (EDX) elemental maps were acquired with a Talos200X microscope (Thermo Fisher Scientific) operated at 200 kV. The samples were prepared on Holey Carbon Film 300 Mesh, Au grids from agar scientific. STEM-EDX maps were acquired in a  $512 \times 512$  px region with a pixel size of 0.256–2.07 nm and a dwell time of 5  $\mu\text{s}/\text{px}$  with a total measurement time of 10 minutes, a collection area of 35–200 mrad, a beam convergence angle of 21–126 mrad and a typical screen current of 1.6 nA with a camera length of 160 mm.

SEM-EDX measurements were performed with Zeiss Leo Gemini 1530 instrument equipped with the secondary electron and back-scattered electron and Inlens detector.

Hydrogen temperature programmed reduction (TPR) of the fresh catalysts was performed in a Microtrac Belcat II instrument with the following temperature program: 5 °C min<sup>-1</sup> (up to 800 °C) using 5 vol%  $\text{H}_2$  in Ar. The same instrument was used for the temperature programmed oxidation measurements (TPO). The following temperature

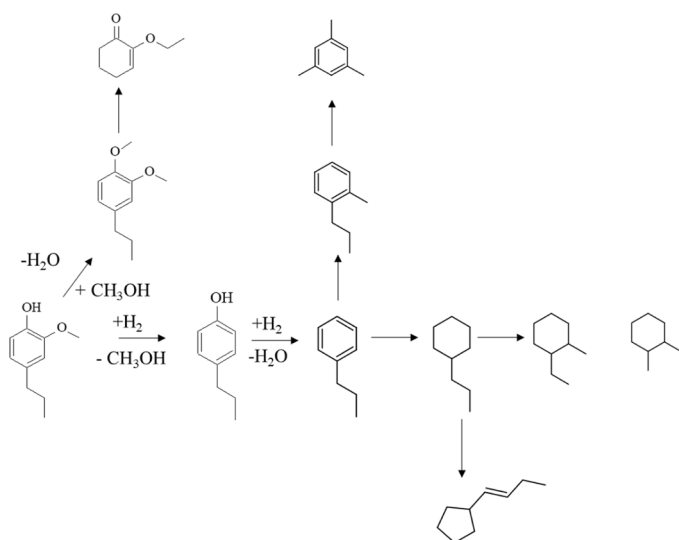


Fig. 1. A simplified reaction network.

program was used: 5 °C/min (up to 900 °C for 10 min) and 2 °C/min (up to 400 °C for 20 min) under 5 vol% oxygen in argon.

The crystalline structure and phase composition of the spent catalysts were investigated by X-ray diffraction (XRD). Preliminary measurements were performed with the wavelength of irradiation of 1.78892 Å (Co K $\alpha$ ) using a DRON-4-0.7 diffractometer. The provided diffraction patterns were collected with Panalytical Aeris diffractometer equipped with PIXcel1D detector using Cu K $\alpha_{1,2}$  (1.5406, 1.5444 Å) radiation. HighScore Plus software and the PDF-4 + database were used for the phase identification [30,31].

Metal contents of the catalysts were determined through Inductively Coupled Plasma Optical Emission Spectroscopy (ICP-OES) (PerkinElmer, Optima 5300 DV). The catalysts were dissolved in a microwave oven using a mixture of sulfuric (3 ml) and nitric (3 ml) acids.

For thermogravimetric analysis of the spent catalysts a TA Instruments SDT 650 instrument was used. The heating rate was 10 °C min<sup>-1</sup> (up to 800 °C for 1 min) in air atmosphere.

To determine the carbon and hydrogen content in the spent catalysts, CHNS analysis was performed at 950 °C using a Thermo Fisher Scientific Flash 2000 organic elemental analyzer equipped and a TC detector. The standards for quantitative determination of elements cystine, 2,5-bis(5-tert-butyl-benzoxazol-2-yl)thiophene, sulphanilamide and methionine were used.

The acidity was measured for the catalyst pellets of ca. 15–20 mg by infrared spectroscopy (ATI Mattson FTIR) using pyridine ( $\geq 99.5\%$ , a. r.) as a probe molecule. For the quantification of the acid sites the molar extinction factors from [32] were used.

*In situ* X-ray absorption spectra (XAS, in terms of XANES and EXAFS) at Fe and Ni K absorption edges were recorded at the P65 beamline of PETRA III synchrotron radiation source (DESY, Hamburg) in the transmission mode. Higher harmonics were rejected by a pair of Si plane mirrors installed in front of the monochromator. The energy of the X-ray photons was selected by a Si (111) double-crystal monochromator and the beam size was set by means of slits to 0.3 (vertical) x 1.5 (horizontal) mm<sup>2</sup>.

For the measurements, the catalyst samples (sieve fraction of 100–200  $\mu\text{m}$ ) were placed in quartz capillaries (1.5 mm o.d., 0.02 mm wall thickness, WJM Glas), sample bed length 3 mm, fixed by quartz wool plugs on both sides. Pure H<sub>2</sub> was flowing through the samples at 30 ml/min flow rate. The samples were heated by a hot air blower from 20 to 250 °C at 2 °C/min ramp rate, held for 2 h at 250 °C and then further heated (the same ramp rate) to 500 °C with a dwell time of additional 2 h. XANES spectra were evaluated by linear combination analysis (LCA) in the range of  $-15$  to  $+35$  eV around the absorption edge.

EXAFS spectra for analysis were measured before the reduction and after cooling to 20 °C, no significant changes (only those related to thermal disorder) were observed during cooling. EXAFS analysis was performed on the spectra measured after reduction and cooling to 20 °C.

X-ray absorption near edge spectra (XANES) were normalized and the extended X-ray absorption fine structure spectra (EXAFS) background subtracted using the Athena program from the IFEFFIT software package [33]. The  $k^2$ -weighted EXAFS functions were Fourier transformed (FT) in the  $k$  range of  $2 - 14 \text{ \AA}^{-1}$  and multiplied by a Hanning window with a sill size of  $1 \text{ \AA}^{-1}$ . The displayed FT EXAFS spectra were not corrected for the phase shift. For the structure refinement amplitude reduction factors  $S_0^2$  0.65 (Fe) and 0.81 (Ni) were obtained by fitting the Fe and Ni foil reference spectra. The fits of the EXAFS data were performed using Artemis [33] by a least square method in  $R$ -space between 1.0 and 3.0 Å. Coordination numbers (CN), interatomic distances ( $r$ ), energy shift ( $\delta E_0$ ) and the mean square deviation of interatomic distances ( $\sigma^2$ ) were refined during fitting. The absolute misfit between the theory and the experiment was expressed by  $\rho$ .

The Fe valence state composition in the bulk was investigated by Mössbauer spectroscopy. The <sup>57</sup>Fe Mössbauer spectra were acquired in transmission geometry at 295 K using an 18-month-old <sup>57</sup>Co:Rh source

(Ritverc Co.) with a maximum Doppler velocity of 11.0 mm s<sup>-1</sup>. For the Mössbauer absorbers 60–80 mg of powder was evenly distributed on an aluminium foil and mixed with an epoxy resin. The circular absorbers had a diameter of 18 mm. The spectra were fitted using the full Hamiltonian of mixed magnetic and electric hyperfine interactions, with the internal field  $B$  (when present), quadrupole coupling constant  $eQV_{zz}$  and isomer shift  $\delta$  as fit parameters. The spectra were fitted with a maximum of three magnetic sextets and three paramagnetic doublets. For the latter components  $B$  was fixed to zero. The linewidth (FWHM) was constrained equal for all paramagnetic doublets and also for the sextets one common linewidth was used. As the magnetic sextets exhibited additional broadening a Gaussian distribution was used for each component with the width  $\Delta B$  used as a free parameter. Small amounts of Fe impurities in the beryllium window of the  $\gamma$  detector were modelled using a paramagnetic doublet and kept fixed during the fittings.

### 2.3. Experimental setup

Solventless hydrodeoxygenation of dihydroeugenol (Sigma Aldrich,  $\geq 99\%$ ) was performed in a tubular reactor with the inner diameter of 4.3 mm and length 50 cm at 300 °C under 30 bar hydrogen (Woikoski, N50, 99.999 %) using 1:15 molar ratio of dihydroeugenol to hydrogen and the weight hour space velocity of 8.4 h<sup>-1</sup>. The residence time of the liquid was 11.6 min. Typically, 0.3 g of the catalyst with the particle size range of 150–180  $\mu\text{m}$  was used being mixed with 0.7 g quartz particles of 250 – 300  $\mu\text{m}$  size. The absence of external mass transfer limitations was already confirmed in [27] while the definitions and equations to calculate conversion, mass balance closure carbon balance in the liquid phase, yields, selectivity, rates and TOF are given in [Supporting information](#). Prior to the reaction, the catalysts were reduced *in situ* to 250 °C for 2 h with 2 °C/min and to 500 °C for 2 h with 2 °C/min.

For analysis of the liquid samples an Agilent 6890 N gas chromatograph (GC) equipped with an FID detector and a DB-1 column (30 m  $\times$  250  $\mu\text{m}$   $\times$  0.5 mm) was used. The following temperature program was applied: 60 °C (5 min) – 138 °C (3 °C/min) – 160 °C (1.5 °C/min) – 300 °C (15 °C/min, 1 min) and the detector temperature was 280 °C. For calibration of the gas chromatographic method the following chemicals were used: dihydroeugenol, hexane, cyclohexane (Alfa Aesar,  $\geq 99.9\%$ ), propylcyclohexane (Sigma, Aldrich, 99 %), 2,5-dimethylhexane (Sigma Aldrich, 99 %) and ethylbenzene (Merck,  $\geq 99.5\%$ ). The products were identified using an Agilent GC/MS 6890 N/5973 and a DB-1 column applying the same temperature program as used for the quantification.

### 2.4. Computational methods

Density functional theory (DFT) calculations were carried out using VASP 6.4.1. Since only metallic catalysts were investigated, a revised PBE functional sufficed for a good description of the semilocal exchange and correlation. The projector augmented wave (PAW) formalism described the interaction between the valence electrons and the stationary nuclei. The electron wave function was cut off at 550 eV. To improve the convergence, a Gaussian smearing of 0.05 eV was applied to the electron occupancies. Magnetic moments were free to assume the lowest energy state, starting from the initial guess of 0.7 eV and 2.7 eV for Ni and Fe, respectively. Computational dipole (along a normal of the slab) corrections and empirical van der Waals corrections (Grimme D3) were also employed. Since very large  $6 \times 6$  supercells were constructed, measuring more than 10 Å in each direction, only gamma point sampling of the reciprocal space was employed.

Geometry optimizations were deemed complete and structure relaxed once the forces on unfrozen atoms decreased to 0.01 eV/Å or lower. While the conjugate gradient method was used when searching for the stable structure, transition states were identified using the dimer method. They were checked by following the reaction path to both directions (reactants, products) and performing vibrational analysis to

ascertain that only one imaginary frequency is present. In all instances, several initial and final positions were probed and the most stable (lowest energy) were considered.

Ni and Fe catalysts were studied as (111) and (110) slabs, respectively, with 6 at. layers, bottom three being fixed in their bulk positions. These were derived from defect-free fcc and bcc structures with unit cell parameters of 3.487 Å and 2.819 Å for Ni and Fe, respectively (experimental values: 3.52 Å and 2.86 Å). To prevent spurious interslab interactions, slabs were separated by 15 Å of vacuum in the *z* direction.

### 3. Results and discussion

#### 3.1. Catalyst characterization results

Morphology of the catalysts was studied with SEM (Fig. S1). For FeNi/USY-30 the particles were of irregular shape with the size in the range from 100 to 1200 nm (Fig. S1a). Furthermore, some large holes can be seen on its surface. FeNi/H-Y-5.1 particles varied in the range of 120–700 nm and had predominantly rectangular shapes (Fig. S1b). In addition, some agglomerates of small particles can be clearly seen. In [34] it was observed that H-Y-5.1 particle size was quite large in comparison to other zeolites. FeNi/H-Beta-38 particles were rather small, 36 nm average size, although some larger particles or agglomerates of ca. 1 µm were also visible (Fig. S1c). It was reported in [35] that the size of the irregular parent H-Beta-38 was ca. 125 nm based on TEM image. For FeNi/H-Beta-300 the particles were of the round shape with the diameter varying in the range of 100–820 nm (Fig. S1d) analogously to [36]. FeNi/Al-MCM-48 exhibits also a very unsmooth surface and an irregular shape (Fig. S1f), with the largest particles or agglomerates of ca. 180 µm size. FeNi/Al<sub>2</sub>O<sub>3</sub> surface is also very unsmooth (Fig. S1h). The particle size of this catalyst varied very much, with the largest agglomerates reaching ca. 140 µm (not depicted here).

EDX analysis (Table 1) showed that Fe and Ni amounts were close to the nominal loading. In addition, the SiO<sub>2</sub>/Al<sub>2</sub>O<sub>3</sub> ratios for FeNi/H-USY-30 and FeNi/H-Beta-38 are close to the nominal ones.

TEM images demonstrate that FeNi/Al<sub>2</sub>O<sub>3</sub> exhibited the smallest metal particles (Fig. 2h, Fig. S2), which can be due to strong interactions of the metal particles with Al<sub>2</sub>O<sub>3</sub> support as also confirmed by hydrogen TPR (see below). The second smallest metal particles can be found in FeNi/H-Y-5.1 which has the highest specific surface area. Smaller particles in FeNi/SiO<sub>2</sub> than for FeNi/H-Beta-300 are probably due to higher surface area of SiO<sub>2</sub>. Overall, because of the cluster size distribution, the sizes are rather close to each other. Smaller metal particles found in FeNi/H-USY-30, FeNi/H-Y-5.1 and FeNi/H-Beta-38 in comparison to FeNi/H-Beta-300 are most probably due to a higher Si/Al ratio of the latter catalyst. The size of FeNi/SiO<sub>2</sub> metal particles were slightly larger

than those of FeNi/H-Beta-300. The size of FeNi/H-Al-MCM-48 catalyst particles was also relatively large 0.8 µm analogously to what was observed for the parent H-Al-MCM-48 in [26].

For the spent catalysts, prominent metal particle sintering occurred for FeNi/H-Beta-300 with a high SiO<sub>2</sub>/Al<sub>2</sub>O<sub>3</sub> ratio (Table 2, Fig. S2-S4). The same was valid for FeNi/SiO<sub>2</sub> while similar to FeNi/H-Beta-300 exhibits very weak interactions between the metal and the support. On the other hand, strongest interactions with the support were confirmed for FeNi/Al<sub>2</sub>O<sub>3</sub> giving a low hydrogen consumption despite its small metal particle size (Table 2). The metal-support interactions discussed here are related to sintering of particles during the experiments and should not be confused with (strong) metal-support interactions in supported metal catalysts resulting in encapsulation of metal nanoparticles by a reducible support (e.g. titania).

Scanning transmission electron microscopy (STEM) combined with energy dispersive X-ray spectroscopy (EDX) mapping was employed to study the proximity of iron and nickel in the supported catalysts. The STEM-EDX maps in Fig. 3 show that in the fresh FeNi on alumina material the elements were well-mixed, resulting in well-dispersed bimetallic Fe-Ni nanoparticles (Fig. 3). For the zeolite supported catalyst, FeNi-Beta-300 the metals appeared substantially more segregated (Fig. S5). Notably, the metal particle size was significantly larger for the zeolite compared to the alumina supported samples, which is in line with the bright field TEM results shown in Fig. 2.

XRD patterns of the spent catalysts (Fig. 6.) reveal that a taenite phase, Fe-Ni alloy with 1:1 ratio [PDF04-005-8641] is most likely present in FeNi/SiO<sub>2</sub> and FeNi/H-USY-30, observed as very small broad peaks at ca. 43.9° and 51.1° 2θ with the average metal particle sizes 10.4 nm and 6.5 nm, respectively. In a similar fashion, the small broad regions in the XRD patterns of FeNi/H-Beta-38 and FeNi/H-Al-MCM-48 close to these angular values could be interpreted as weakly crystalline nanoparticles of Fe-Ni, while no indication of this phase is observed for FeNi/Al<sub>2</sub>O<sub>3</sub>. The formation of taenite (Fe<sub>0.5</sub>Ni<sub>0.5</sub>) is expected on the basis of an earlier report, where, during reduction at 500 °C with hydrogen, both taenite (fcc phase) and kamacite (bcc phase) were observed, particularly with smaller Ni concentrations [37]. It is noteworthy, that in our case only taenite, but not the kamacite phase, was detected. It was also reported in [38] using in-situ XRD that the diffraction peak of Ni(111) at 44.4° 2θ gradually shifted towards lower angles during catalyst reduction at a higher temperature, when iron diffused into nickel lattice causing increase in lattice parameters. Another structure of an Fe<sub>0.9</sub>Ni<sub>0.1</sub> alloy [PDF 04-004-8511] is possibly present in the spent FeNi/H-Y-5.1, but this is rather speculative since the peaks that correspond to this phase are weak and partially overlap with the other phases.

Quartz is present in several samples as an impurity [PDF

**Table 1**

SEM-EDX results (wt%). In parenthesis is the metal contents determined by ICP-OES.

Catalyst	Al	Si	Fe	Ni	O	Fe/Ni	SiO <sub>2</sub> /Al <sub>2</sub> O <sub>3</sub> <sup>b</sup>
FeNi/H-USY-30	2.18	34.32	5.30 (4.71)	5.29 (4.67)	52.91	1.0 (1.0)	30.7
FeNi/H-Y-5.1	1.98	34.30	5.53 (4.70)	5.09 (4.70)	53.10	1.1 (1.0)	33.8
FeNi/H-Beta-38	1.64	34.58	5.48 (4.76)	5.14 (4.65)	53.16	1.1 (1.0)	41.2
FeNi/H-Beta-300	0.43	35.13	4.56 (4.50)	4.45 (4.70)	55.44	1.0 (0.96)	159.6
FeNi/H-Al-MCM-48	1.09	34.84	4.86 (4.41)	5.06 (4.32)	54.15	0.96 (1.0)	30.7
FeNi/SiO <sub>2</sub>	0.13	35.83	4.82 (4.72)	4.87 (4.62)	54.35	1.0 (1.0)	n.a.
FeNi/Al <sub>2</sub> O <sub>3</sub>	39.80 (37.41 <sup>a</sup> )	0 (3.71 <sup>a</sup> )	5.42 (4.71) (4.49 <sup>a</sup> )	5.41 (4.67) (4.69 <sup>a</sup> )	49.37 (43.44 <sup>a</sup> )	1.0 (1.0)	n.a.

<sup>a</sup> spent catalyst, balanced with carbon, which content is 5.96

<sup>b</sup> molar ratio



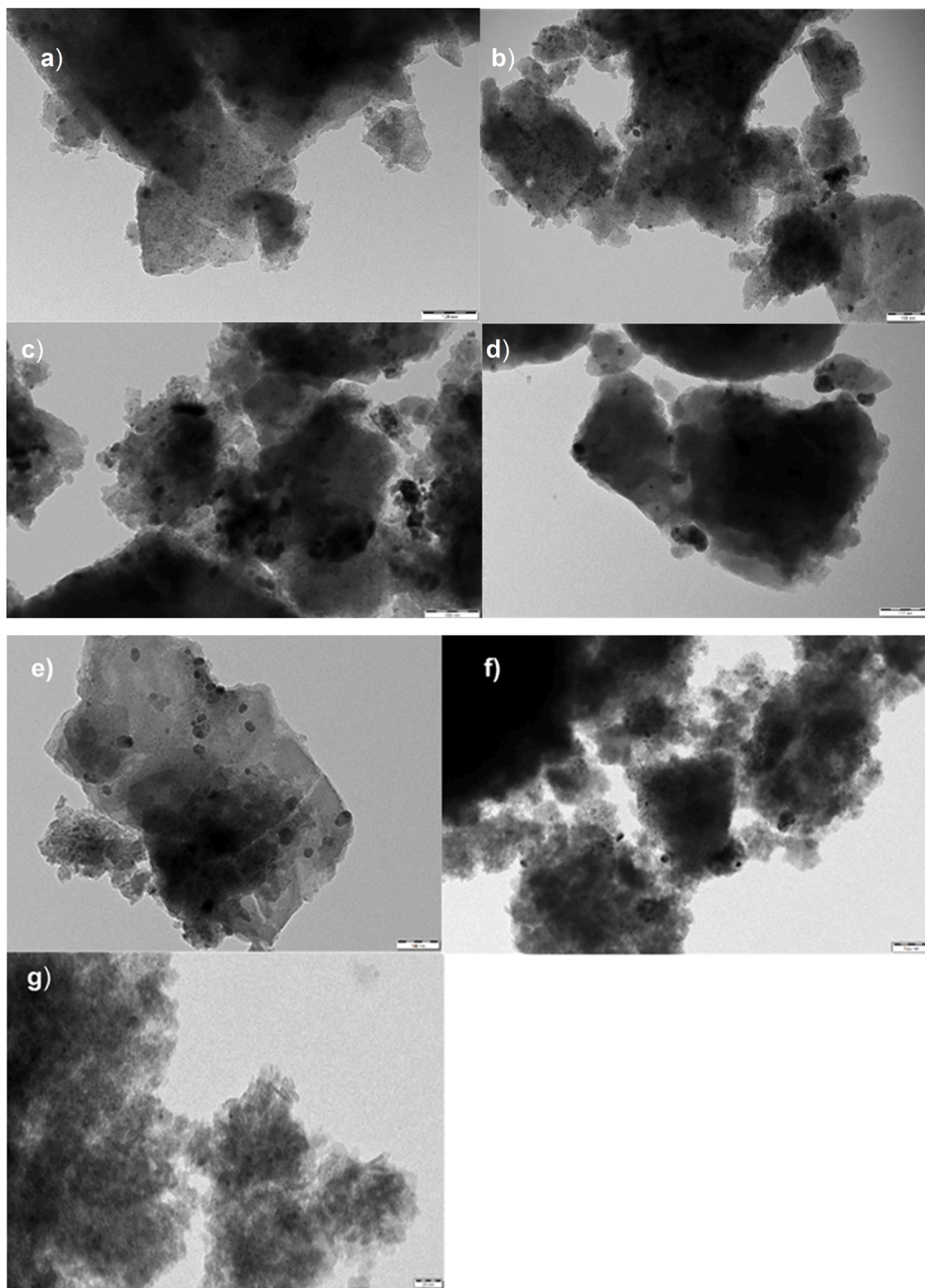


**Fig. 2.** TEM images of the reduced a) FeNi/H-USY-30, b) FeNi/H-Y-5.1, c) FeNi/H-Beta-38, d) FeNi/H-Beta-300, e) FeNi/H-Al-MCM-48, f) FeNi/SiO<sub>2</sub>, and g) FeNi/Al<sub>2</sub>O<sub>3</sub>. Scale 100 nm, for FeNi/Al<sub>2</sub>O<sub>3</sub> 20 nm.

04–005–4718], because the catalysts were loaded with quartz into the reactor. The graphite peak [PDF 00–056–0160] was observed for the spent FeNi/H-Y-5.1 and in FeNi/H-Al-MCM-48, while no graphite phases were observed in the XRD patterns of the other spent catalysts although they contained carbon based on TGA analysis (see below). The XRD patterns show the following supports to be present in the spent

catalysts:  $\gamma$ -Al<sub>2</sub>O<sub>3</sub> [PDF 04–016–1445] with low crystallinity, the beta zeolite [PDF 00–056–0467] in FeNi/H-Beta-38 catalyst with its typical peaks of at 7.8° and 22.4° 2 $\theta$  corresponding to the 101 and 302 planes [39]. For the parent Na-MCM-48 the main peaks are at ca. 3.59° and 4.19° 2 $\theta$  as reported in our previous publication [26] and by Schmidt et al. [40]. These peaks are not observable since the diffraction patterns

**Table 2**

Average metal particle size and dispersion for different fresh and spent FeNi catalysts based on TEM. Sintering degree was defined as  $SD = \frac{d_{spent} - d_{fresh}}{d_{fresh}} \times 100\%$ , in which  $d$  is metal data particle size.

Catalyst	d (nm)	D (%)	SD (%)
FeNi/H-USY-30	6.1 (6.5)	18 (17)	7
FeNi/H-Y-5.1	4.5 (5.1)	24 (21)	13
FeNi/H-Beta-38	5.3 (6.8)	20 (16)	28
FeNi/H-Beta-300	7.5 (15.2)	14 (7)	> 100
FeNi/H-Al-MCM-48	5.0 (4.5)	22 (24)	10
FeNi/SiO <sub>2</sub>	5.9 (10.4)	18 (10)	76
FeNi/Al <sub>2</sub> O <sub>3</sub>	3.4 (4.1)	32 (24)	21

were collected in the 5° to 100° 2θ range. Na-MCM-48 and SiO<sub>2</sub> supports show similar amorphous features at ca. 22° and 44° 2θ.

Textural properties determined by nitrogen adsorption method are summarized in Fig. S6 and Table 3. A broad hysteresis loop ranging from 0.6 up to 1 p/p<sup>0</sup> for FeNi/Al<sub>2</sub>O<sub>3</sub> indicates a broad pore size distribution (Fig. 6m, n) as also reported for Ni/γ-Al<sub>2</sub>O<sub>3</sub> [41]. For the microporous catalysts the highest fraction of mesopores was observed for FeNi/H-USY-30. For FeNi/H-Al-MCM-48 both micro- and mesopores were observed (Fig. S6i,j) with the hysteresis between 0.46 and 0.96 p/p<sup>0</sup>. The surface area of FeNi/H-USY-30 decreased by 19 % after loading the support with ca. 10 wt% metals (Table S1). The results show that the ratio of micro-to-mesopore volume decreased in the following order: FeNi/H-Beta-300 > FeNi/H-Y-5.1, FeNi/H-Beta-38 > FeNi/H-USY-30 > FeNi/H-Al-MCM-48 > FeNi/SiO<sub>2</sub>, FeNi/Al<sub>2</sub>O<sub>3</sub> (0.1). The hysteresis loop between adsorption and desorption branches is clearly visible for the Fe-Ni mesoporous catalysts supported on H-Al-MCM-48, SiO<sub>2</sub> and Al<sub>2</sub>O<sub>3</sub> (Fig. S6). The specific surface area of the parent H-Al-MCM-48 was 719 m<sup>2</sup>/g<sub>cat</sub> [26], while as a comparison for H-Al-MCM-48 with SiO<sub>2</sub>/Al<sub>2</sub>O<sub>3</sub> ratio of 25 the specific surface area and pore diameter were 1247 m<sup>2</sup>/g<sub>cat</sub> and 2.4 nm, respectively [42]. Some mesoporosity is also visible for the metal modified zeolites.

The highest decrease of the specific surface area (SSA) in the spent catalysts was observed for FeNi/H-Beta-38, which exhibited the highest amount of strong Brønsted acid sites (see below), promoting cracking. Interestingly the second highest decrease of SSA was determined for mesoporous, mildly acidic FeNi/H-Al-MCM-48 followed by FeNi/USY-30 and FeNi/H-Y-5.1 which contain also large amounts of Brønsted acid sites. As expected, a lower decrease of SSA was found for FeNi/H-Beta-300 with mild acidity. Mesoporous FeNi/Al<sub>2</sub>O<sub>3</sub> and FeNi/SiO<sub>2</sub> exhibited a rather low decrease of SSA, most probably due to their large pores being also above 5 nm (Fig. S6).

The results from the acidity measurements by the pyridine adsorption-desorption method are shown in Table 4. It can be clearly seen that the loading of metals decreased acidity especially the

concentration of strong Brønsted acid sites (Table 4, Table S2), which was also earlier reported in [43,44]. For metal modified zeolites and FeNi/H-Al-MCM-48 the Brønsted to Lewis acid site ratio decreased substantially, especially by diminishing strong Brønsted acid sites during the metal modification as stated above and also by enhancing the amount of Lewis acid sites, which originate from the ionic metal species, i.e. Ni<sup>2+</sup>, Fe<sup>3+</sup> [45]. Interestingly, the amount of Lewis acid sites increased for FeNi/USY-30, FeNi/H-Y-5.1, FeNi/H-Beta-38 and FeNi/H-Beta-300 in comparison to the parent supports in the range of 26–68 % [35,46,47]. However, the opposite was observed for the mesoporous catalysts FeNi/H-Al-MCM-48, FeNi/SiO<sub>2</sub>, FeNi/Al<sub>2</sub>O<sub>3</sub>, with the corresponding decrease of 72 %, 3 % and 34 %, respectively [26,48–50] (Table 4, Table S2). For microporous catalysts most of iron and nickel remains on the outer surface of the supports, as based on TEM measurements.

The amounts of metals in catalysts determined by ICP-OES given in Table 5 illustrate that the content of Fe and Ni is close to the nominal ones.

The results for hydrogen uptake determined by TPR of the fresh catalysts (Fig. 5, Table 6) indicate that the hydrogen uptake of the metals during TPR decreased in the following order: FeNi/H-Beta-300 > FeNi/H-Beta-38 = FeNi/SiO<sub>2</sub> > FeNi/USY-30 > FeNi/H-Y-5.1 > FeNi/Al-MCM-48 > FeNi/Al<sub>2</sub>O<sub>3</sub>. The low reducibility of FeNi/Al<sub>2</sub>O<sub>3</sub> is explained by the strong interactions between Ni and Al<sub>2</sub>O<sub>3</sub> [51] as well as formation of NiAl<sub>2</sub>O<sub>4</sub> as observed for this catalyst by XAS (see below). NiAl<sub>2</sub>O<sub>4</sub> is reducible, according to the literature, above 500 °C in line with the current results [52]. The peak for hydrogen consumption around 395 °C is related to reduction of Fe(III) to Fe(II) [53]. As a comparison, the maximum peaks for hydrogen consumption for FeNi/Al<sub>2</sub>O<sub>3</sub> were 375 °C and 602 °C in the current case and for 5Ni5Fe on Al<sub>2</sub>O<sub>3</sub> prepared by the incipient wetness method the corresponding maximum hydrogen peaks were found at 387 °C and 517 °C [51] being close to those observed in the current work. A relative hydrogen uptake increased with the increasing metal particle size (Fig. 6) analogously to various Ni-Fe catalysts supported on mesoporous carbon spheres [54]. For mesoporous silica, when the metal particles have weak interactions with the support, a high hydrogen uptake can be also observed (Table 6). Analogously to [51], a higher degree of metal reduction than for FeNi/Al<sub>2</sub>O<sub>3</sub> was obtained for FeNi/SiO<sub>2</sub>. In addition, for zeolites with the metal particles locating in the outer surface of the support a relatively high hydrogen uptake can be detected. A slightly lower hydrogen uptake was measured for the mesoporous FeNi modified H-Al-MCM-48, which also contains aluminium, where a part of the metal particles is possibly located inside the support pore structure. The TPR data are similar to [55] in which TPR of 10 % Ni-5 % Fe/Al-MCM-48 was studied giving two temperature maxima at 400 °C and 530 °C. In [56] the metal particle size for 10 % Ni-5 % Fe/Al-MCM-48 was 7 nm, somewhat larger than in the current case of 5 nm. It was additionally observed in [55]

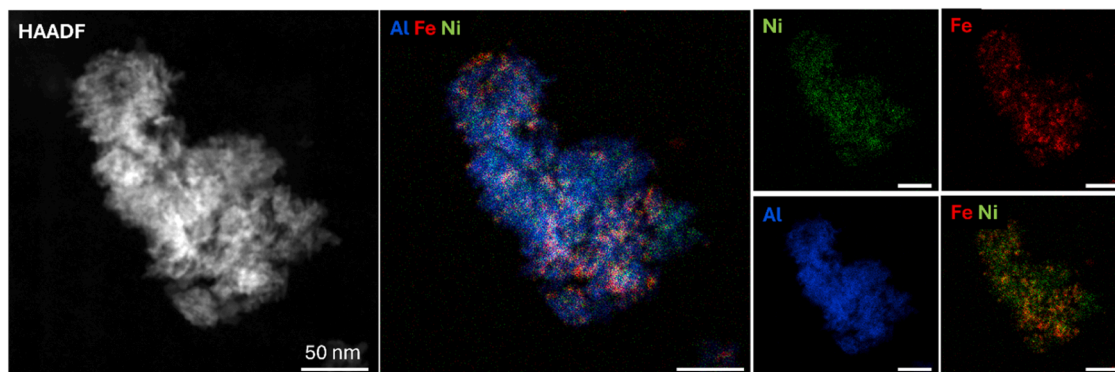


**Fig. 3.** HAADF-STEM and STEM-EDX images of the fresh FeNi/Al<sub>2</sub>O<sub>3</sub> catalysts. Iron, nickel and aluminium are shown in red, yellow and blue, respectively. All scale bars are 50 nm.

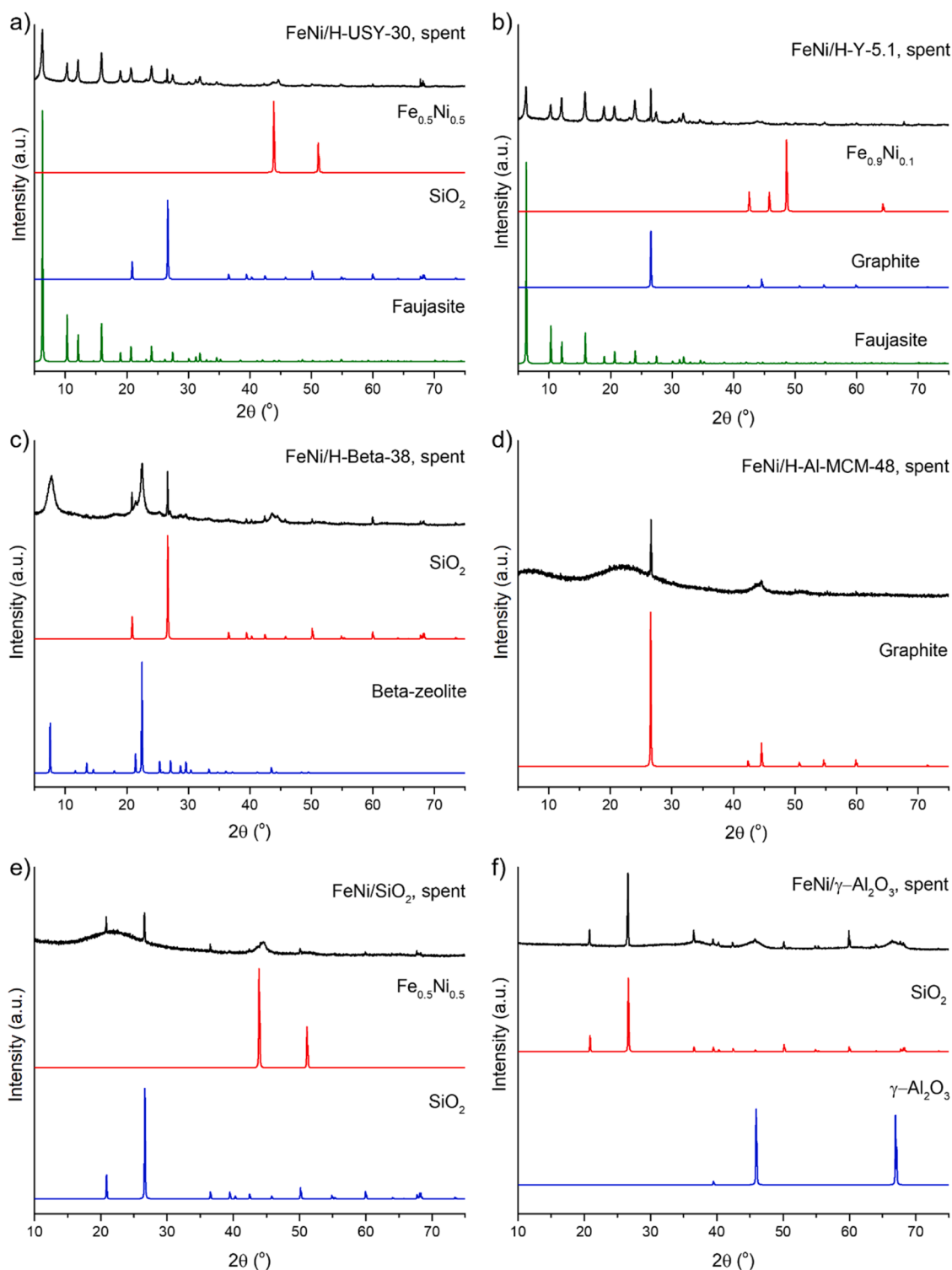


**Fig. 4.** Diffractograms for spent a) FeNi/H-USY-30, b) FeNi/H-Y-5.1, c) FeNi/H-Beta-38, d) FeNi/H-Al-MCM-48, e) FeNi/ $\text{SiO}_2$  and f) FeNi/ $\text{Al}_2\text{O}_3$ .

that a higher metal dispersion gives stronger interactions with the support as could be anticipated. The low temperature peak maximum for hydrogen uptake is the lowest for FeNi/ $\text{SiO}_2$  followed by FeNi/H-Beta-300 which also indicates that in the presence of a small amount of aluminium in FeNi/H-Beta-300 there are some weak interactions of the metal particle with the support.

Room-temperature Mössbauer spectra are displayed in Fig. 7 with the amount of different iron species determined from Mössbauer spectroscopy given in Table 7. The iron traces found as an impurity in the

detector windows are drawn in Fig. 7 using a dashed black line. All spectra except the one measured for FeNi/ $\text{Al}_2\text{O}_3$  (Fig. 7 h) exhibit magnetic sextets. The experimentally obtained internal field of the sextets correspond rather well to the  $\sim 33$  T internal field of metallic Fe. Broadening, due to iron having a varying number of Ni neighbours, is observed and in some cases 1–2 additional sextets (drawn in light green and lime) are needed to properly fit the data. It is surmised that the additional sextets with a smaller field and a larger broadening are due to iron with very few next-neighbour Fe atoms. Only two of the spectra

**Table 3**

Textural properties of the catalytic materials. In parenthesis values for the spent catalyst. dSA means a decrease of the surface area during reaction (%).

Catalyst	SA (m <sup>2</sup> g <sup>-1</sup> ) D-R	dSA (%)	d <sup>a</sup> (nm)	V <sub>mic</sub> (cm <sup>3</sup> g <sup>-1</sup> )	V <sub>mes</sub> (cm <sup>3</sup> g <sup>-1</sup> )	V <sub>T</sub> (cm <sup>3</sup> g <sup>-1</sup> )	V <sub>mic</sub> /V <sub>mes</sub>	Mesoporosity (%)
FeNi/H-USY-30	619 (164)	-74	0.84 (0.55–0.8)	0.22	0.09	0.31	2.44	29
FeNi/H-Y-5.1	662 (143)	-78	0.84 (0.55)	0.24	0.08	0.32	3.0	25
FeNi/H-Beta-38	503 (27)	-95	0.66 (0.84)	0.21	0.07	0.28	3.0	25
FeNi/H-Beta-300	516 (143)	-72	0.66 (0.66)	0.21	0.05	0.26	4.2	19
FeNi/H-Al-MCM-48	273 (44)	-84	0.66, 2.9 (3.8)	0.07	0.10	0.17	0.7	59
FeNi/SiO <sub>2</sub>	206 (140)	-32	5–17 (2.4–12)	0.04	0.39	0.43	0.10	91
FeNi/Al <sub>2</sub> O <sub>3</sub>	180 (99)	-45	2.4–20, (2.4–13.6)	0.04	0.49	0.53	0.08	92

<sup>a</sup> large pore volume at the given pore size**Table 4**

Catalytic acidity results determined by pyridine adsorption-desorption.

Catalyst	Brønsted acidity (μmol g <sup>-1</sup> )				Lewis acidity (μmol g <sup>-1</sup> )				Total (μmol g <sup>-1</sup> )	BA/LA ratio
	Weak	Medium	Strong	Total	Weak	Medium	Strong	Total		
FeNi/USY-30	30	106	0	136	47	24	0	71	207	1.91
FeNi/H-Y-5.1	43	59	0	102	74	11	0	86	158	1.19
FeNi/H-Beta-38	10	117	13	141	69	72	4	146	286	0.96
FeNi/H-Beta-300	24	23	0	47	34	23	0	57	104	0.82
FeNi/H-Al-MCM-48	11	14	0	25	45	5	0	50	74	0.49
FeNi/SiO <sub>2</sub>	4	5	0	9	3	2	0	4	13	1.92
FeNi/Al <sub>2</sub> O <sub>3</sub>	37	0	0	37	92	28	0	122	158	0.30

**Table 5**

Amounts of metals in the catalysts determined by ICP-OES.

Catalyst	Fe (wt%)	Ni (wt%)
FeNi/USY-30	4.71	4.67
FeNi/H-Y-5.1	4.70	4.70
FeNi/H-Beta-38	4.76	4.65
FeNi/H-Beta-300	4.50	4.70
FeNi/H-Al-MCM-48	4.41	4.32
FeNi/SiO <sub>2</sub>	4.72	4.62
FeNi/Al <sub>2</sub> O <sub>3</sub>	4.71	4.67

exhibit signature of the divalent iron (indicated in blue in Fig. 7b and h), with a typically large isomer shift and a non-zero quadrupole splitting. In addition to these, paramagnetic doublets formally compatible with trivalent iron (drawn in red, orange and brown) are seen in all spectra. However, previous measurements have shown that a part of the “trivalent” Fe orders magnetically and adds to the sextets of metallic Fe at lower temperatures [56]. Therefore, assigning these doublets to trivalent Fe should be done with caution. It should be also mentioned that for a fair interpretation of the Mössbauer spectroscopy results it should be kept in mind that some surface oxidation of especially iron species could have occurred upon catalyst exposure to air prior to measurements.

The relative hydrogen uptake of different catalysts determined by hydrogen TPR is increasing with the fraction of metallic iron determined by Mössbauer spectroscopy and listed in Table 7. At the same time the average metal particle size increased with increasing metallic iron content (Fig. 8).

XANES spectra of the catalysts are shown in Fig. 9. Fe species in all as-received catalysts display XANES spectra with similar features as the maghemite (γ-Fe<sub>2</sub>O<sub>3</sub>) reference spectrum, however, with significant broadening for FeNi/H-Y-5.1 and FeNi/Al<sub>2</sub>O<sub>3</sub>, qualitatively suggesting a similar oxidation state and a local coordination environment around Fe sites but lack of long-range ordering. Ni XANES spectrum suggests NiO in case of FeNi/H-Beta-300 and partially disordered NiO for FeNi/H-Y-5.1, while Ni<sup>2+</sup> incorporated in the structure of NiAl<sub>2</sub>O<sub>4</sub> spinel is proposed for the FeNi/Al<sub>2</sub>O<sub>3</sub> catalyst.

Fe K and Ni K edge positions in the spectra of the reduced FeNi/H-Y-5.1 and FeNi/H-Beta-300 catalysts correspond to that of the reference metal spectra, hence both Fe and Ni metals are fully reduced after

hydrogen pretreatment. However, oscillations above the Fe K edge in the reduced FeNi/H-Y-5.1 and FeNi/Beta-300 do not correspond to that of bcc Fe metal (Fe foil) and spectra qualitatively resemble spectra of fcc metals such as Ni, signifying formation of FeNi alloy.

Ni K edge spectrum of the reduced FeNi/H-Y-5.1 catalyst can be fitted as  $0.95 \pm 0.02$  Ni metal and  $0.05 \pm 0.02$  Ni<sup>2+</sup> components, while Fe species are more oxidized and can be fitted as a mixture of  $0.6 \pm 0.02$  Fe<sup>0</sup> (in form of FeNi alloy),  $0.25 \pm 0.02$  FeO, and  $0.15 \pm 0.02$  Fe<sub>3</sub>O<sub>4</sub>.

Ni K edge spectrum of the reduced FeNi/Al<sub>2</sub>O<sub>3</sub> catalyst exhibits a mixture of Ni metal and Ni<sup>2+</sup> components, the corresponding molar fractions as determined by the linear combination analysis are  $0.36 \pm 0.01$  NiAl<sub>2</sub>O<sub>4</sub> and  $0.64 \pm 0.01$  Ni<sup>0</sup>. Fe K edge spectrum of the reduced FeNi/Al<sub>2</sub>O<sub>3</sub> catalyst can be fitted as a linear combination of  $0.63 \pm 0.03$  Fe<sub>3</sub>O<sub>4</sub> and  $0.37 \pm 0.03$  Fe<sup>0</sup>, where Fe<sup>0</sup> component fits to the FeNi alloy rather than bcc Fe foil spectrum.

Fourier transformed EXAFS spectra and the respective fits are depicted in Fig. 10, Fig. S7–S10. It can be concluded from the XANES analysis that Fe species (Fig. 10, left) in the fresh FeNi/H-Beta-300 catalyst correspond to bulk maghemite, while scattering on the second and further shells in FeNi/H-Y-5.1 and FeNi/Al<sub>2</sub>O<sub>3</sub> is weaker suggesting high dispersion of Fe especially on alumina, possibly with formation of Fe aluminate. Ni species in the fresh catalysts correspond to bulk (FeNi/H-Beta-300) and partially disordered (FeNi/H-Y-5.1) NiO as well as Ni aluminate in case of FeNi/Al<sub>2</sub>O<sub>3</sub>.

After reduction only scattering on metal nearest neighbours in the first coordination shell (uncorrected distance of ca. 2.2 Å) can be seen in the Fe K spectra of FeNi/H-Beta-300 and FeNi/H-Y-5.1. Noteworthy, the coordination environment around Fe atoms in the reduced FeNi/H-Beta-300 and FeNi/H-Y-5.1 catalysts does not correspond to bcc Fe reference spectrum (especially visible for further shells at 3.5–5 Å uncorrected distance) but shows similarities to fcc Ni spectra. This is in line with the corresponding XANES analysis which identified fcc FeNi alloy formation. Ni K edge XANES spectra show exclusively fcc metallic structure in all reduced catalysts, scattering amplitude is significantly lower for the FeNi/Al<sub>2</sub>O<sub>3</sub> catalyst which may be due to both a mixture of species and a nanosizing effect.

Fe K edge EXAFS spectrum of the reduced FeNi/Al<sub>2</sub>O<sub>3</sub> catalyst shows some scattering on metal atoms at approx. 2.1 Å with a rather low intensity, signifying small reduced nanoparticles. At the same time, the backscattering peak between 1 and 2 Å points at incomplete reduction of Fe.



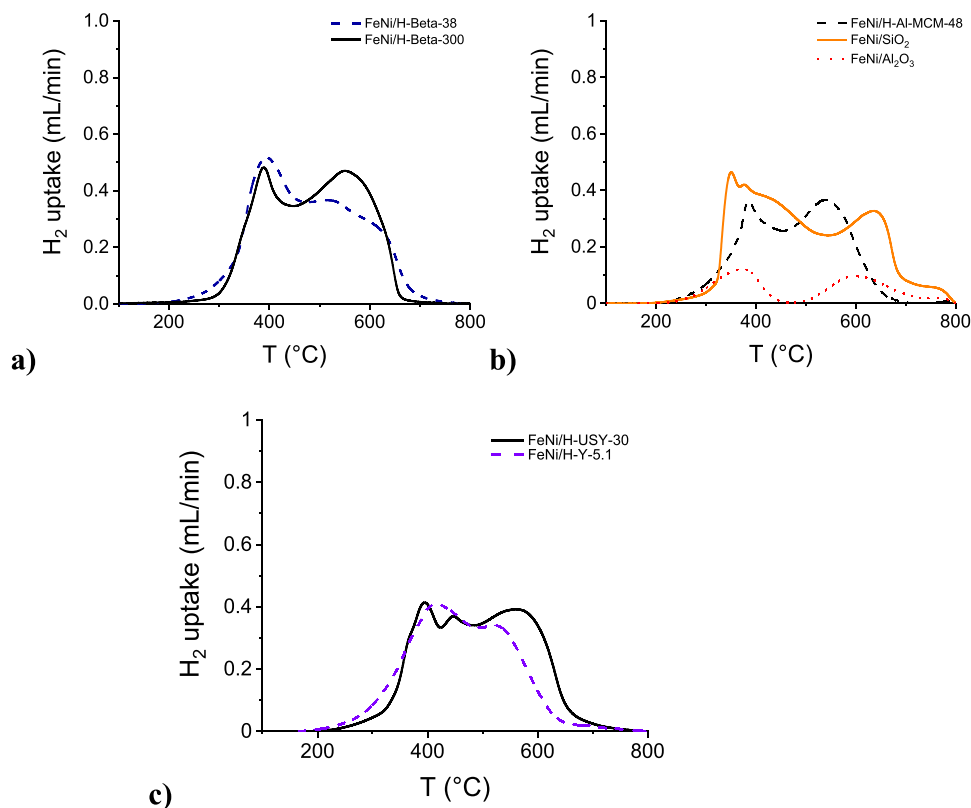
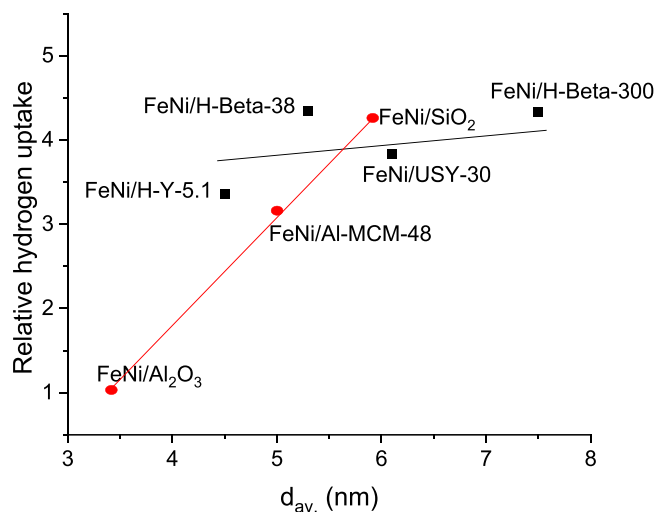


Fig. 5. Hydrogen TPR results of different catalysts.

Table 6

Hydrogen TPR results. The relative hydrogen uptake has been taken in comparison to hydrogen uptake of FeNi/Al<sub>2</sub>O<sub>3</sub>.

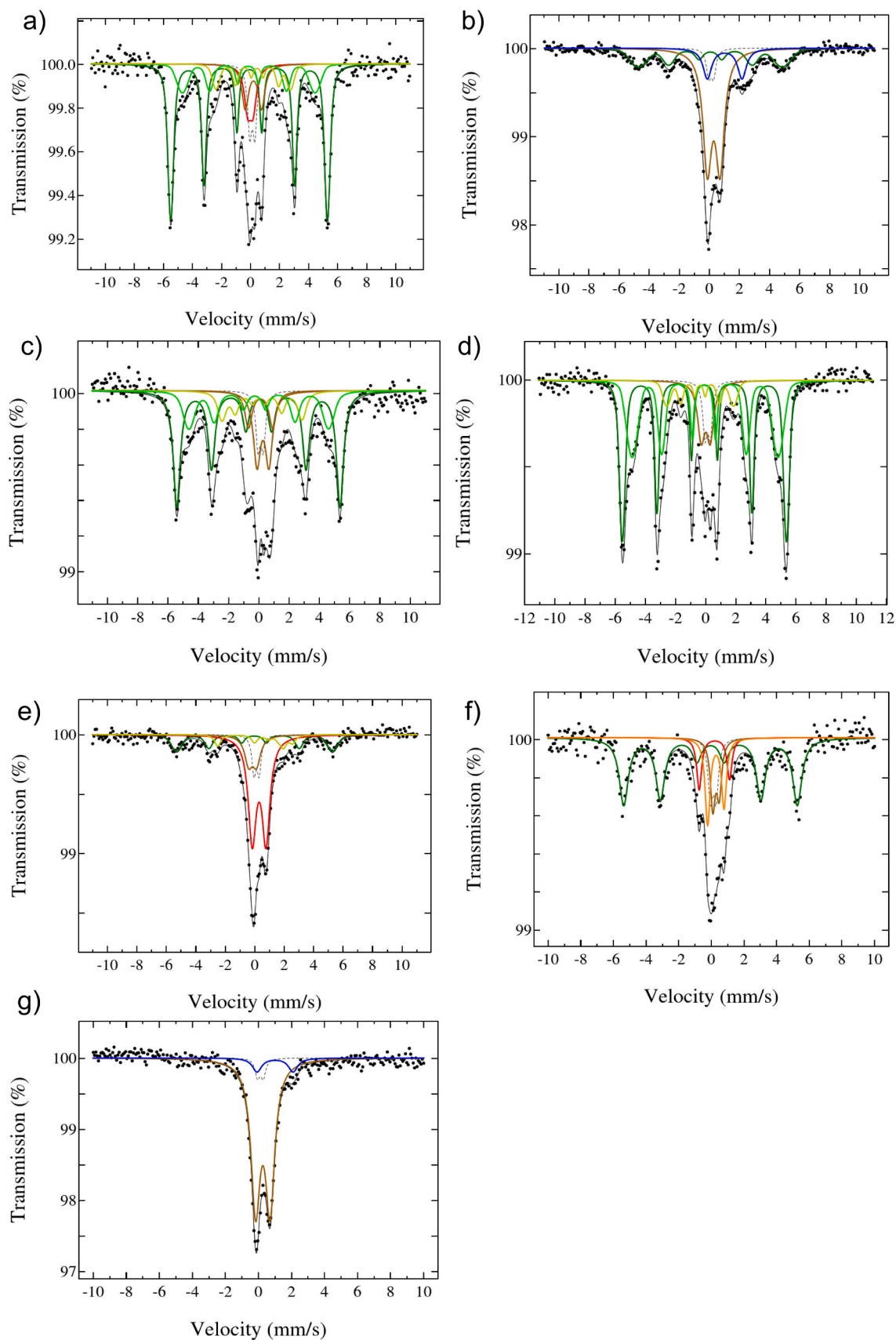
Catalyst	T <sub>max1</sub> (°C)	T <sub>max2</sub> (°C)	T <sub>max3</sub> (°C)	T <sub>max4</sub> (°C)	H <sub>2</sub> μmol/metal μmol (%)	Relative H <sub>2</sub> uptake
FeNi/USY-30	395	446	562	n.a.	79	3.84
FeNi/H-Y-5.1	390	460	550	630	70	3.36
FeNi/H-Beta-38	395	520	620	n.a.	89	4.35
FeNi/H-Beta-300	360	550	n.a.	n.a.	92	4.34
FeNi/H-Al-MCM-48	386	541	n.a.	n.a.	69	3.16
FeNi/SiO <sub>2</sub>	351	379	442	640	89	4.27
FeNi/Al <sub>2</sub> O <sub>3</sub>	375	602	n.a.	n.a.	21	1.0

Fig. 6. Relative hydrogen consumption in comparison to hydrogen uptake of FeNi/Al<sub>2</sub>O<sub>3</sub> as a function of the average metal particle size in FeNi catalysts and the metal particle size.

To obtain quantitative structural information on the reduced Fe and Ni species EXAFS refinement was performed (Table 8). In the case of the reduced FeNi/H-Beta-300 catalysts two independently made fits at Fe and Ni K edges resulted in exactly the same structural parameters with the coordination numbers (CN) of approximately 11. This CN corresponds to rather large, on the order of 3–10 nm (with large error bars due to uncertainty in CN determination and asymptotic behaviour of the model [57]) fcc FeNi nanoparticles. The same CN around Ni and Fe suggest a random distribution of both metals in the alloy.

As follows from XANES, degrees of reduction of Ni and Fe in FeNi/H-Y-5.1 are different with ca. 95 % of reduced Ni and ca. 60 % of reduced Fe (in form of fcc. FeNi). As a comparison, a degree of iron reduction based on ex situ Mössbauer spectroscopy was 30 % (Table 8). It should be kept in mind as mentioned above that for XANES measurements the reduction was made in situ, while some surface oxidation of iron species could happen prior to Mössbauer spectroscopy measurements upon catalysts exposure to air.

If one looks at the CN around Ni, the particle sizes are similar to the FeNi/H-Beta-300. CN around Fe is lower than CN around Ni, however Fe is partially oxidized as also confirmed by the Mössbauer spectroscopy (Table 8). If one assumes a mixture of a separate oxide and metallic Fe species and corrects CN (Fe-Fe) by the extent of reduction, a physically

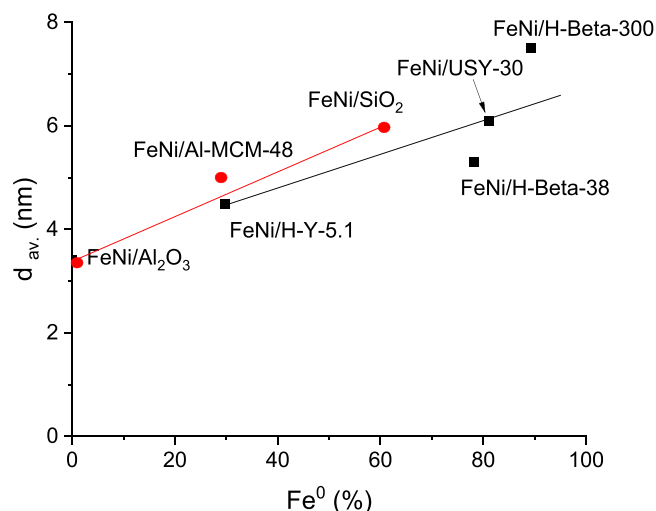


**Fig. 7.**  $^{57}\text{Fe}$  Mössbauer spectra for different reduced catalysts: a) FeNi/H-USY-30, b) FeNi/H-Y-5.1, c) FeNi/H-Beta-38, d) FeNi/H-Beta-300, e) FeNi/H-Al-MCM-48, f) FeNi/SiO<sub>2</sub> and g) FeNi/Al<sub>2</sub>O<sub>3</sub>.

**Table 7**

Amount of different iron species determined from Mössbauer spectroscopy.

Catalyst	Fe <sup>0</sup> (%)	Fe <sup>3+</sup> (%)	Fe <sup>2+</sup> (%)
FeNi/H-USY-30	81.0	19.0	0
FeNi/H-Y-5.1	29.8	56.2	14.1
FeNi/H-Beta-38	78.1	21.9	0
FeNi/H-Beta-300	89.2	10.7	0
FeNi/H-Al-MCM-48	29.2	70.8	0
FeNi/SiO <sub>2</sub>	60.8	39.3	0
FeNi/Al <sub>2</sub> O <sub>3</sub>	0	94.1	4.9

**Fig. 8.** Average metal particle size as a function of metallic Fe content in the catalyst. Notation: Microporous catalysts (■), mesoporous catalysts (●).

unreasonable value CN = 13.3 is obtained proving the assumption false. Hence, the oxidized Fe species may be located on the surface of FeNi nanoparticles.

Degrees of reduction of Ni and Fe in FeNi/Al<sub>2</sub>O<sub>3</sub> are also different being ca. 64 % for Ni and ca. 37 % for Fe (in the form of fcc FeNi). Unreduced Ni is stabilized in NiAl<sub>2</sub>O<sub>4</sub> phase and is probably not in the direct contact with reduced Ni NPs. If this assumption is true, the corrected CN (Ni-Ni) would be ca. 11.8. Correcting CN (Fe-Fe) by the extent of reduction results in a very low value of ca. 6.8. Hence, there is definitely no random distribution of Fe and Ni in the bimetallic alloyed FeNi NPs but rather Fe-rich surface and Ni-rich core. In such a case a reliable estimation of the particle size is not possible.

When comparing the results of the reduced catalysts studied by

XANES spectra and the spent ones by XRD, it can be observed that Ni-Fe alloy was observed for FeNi/H-Y-5.1 by both methods. XANES spectrum confirmed presence of FeNi alloy and NiAl<sub>2</sub>O<sub>4</sub> in FeNi/Al<sub>2</sub>O<sub>3</sub>, which were not confirmed by XRD most probably due to their small sizes (Table 9). In addition, an alloy was present in FeNi/H-Beta-300, as confirmed by XANES. A degree of iron reduction determined by XANES spectra for FeNi/H-Y-5.1 was 37 %, which was close to that determined by performed ex situ Mössbauer spectroscopy being 29.8 % (Table 7).

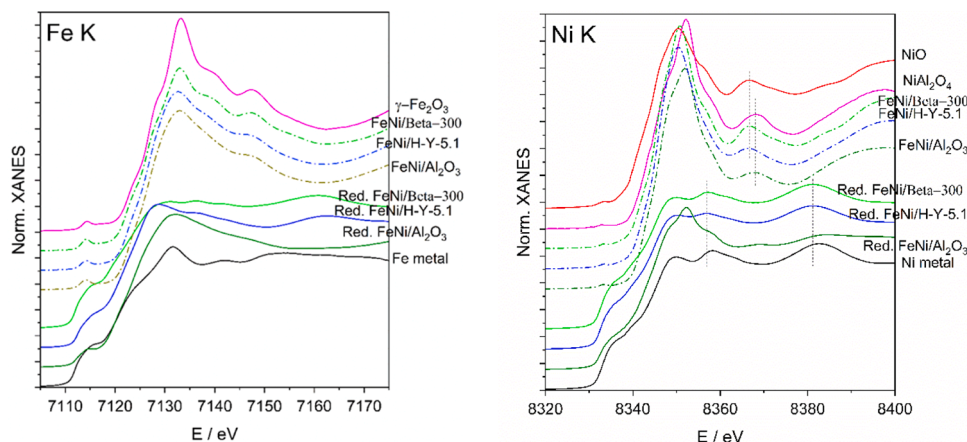
Coke formation and the temperature for the maximum heat release were determined by TGA for different spent catalysts (Table 10, Fig. S11 and S12). The results show that the highest amount of coke after 6 h TOS was determined for the FeNi/H-Beta-300 followed by FeNi/H-Y-5.1, while for the other catalysts the coke amounts were below 5 wt% and the smallest amount of coke was detected for FeNi/Al<sub>2</sub>O<sub>3</sub>. Interestingly, also for FeNi/Al<sub>2</sub>O<sub>3</sub> the TGA profile demonstrated that the weight loss was higher from the fresh than from the spent one. A potential explanation could have been some thermal degradation of the metastable structure of alumina produced by UOP for the fresh catalyst [58]. On the other hand, the metastable phases should have already been converted to stable phases upon calcination at 450 °C during catalyst preparation. Currently, it can be only speculated what is the potential reason for the observed behaviour.

The rate for coke formation is calculated as the mass of coke formed during the experiment divided by the total time-on-stream and plotted as a function of the degree of mesoporosity of the catalyst (Fig. 11). The results show that the amount of coke in the spent catalyst in general decreased with increasing mesoporosity as expected.

As a comparison, the corresponding coke formation rate using the same NiFe/H-Beta-300 as a catalyst for isoeugenol was reported to be 37 μg<sub>coke</sub>/g<sub>cat</sub>/h [27] under similar conditions, therefore the double bond in isoeugenol has a prominent effect on the catalyst coking rate.

The amount of coke was also correlating with the fraction of Fe<sup>3+</sup> species in the reduced fresh catalysts determined by Mössbauer spectroscopy for the mesoporous catalysts. When the fraction of Fe<sup>3+</sup> decreased, the amount of coke increased as follows: FeNi/Al<sub>2</sub>O<sub>3</sub> > FeNi/H-Al-MCM-48 > FeNi/SiO<sub>2</sub> analogously to [59] (Fig. 12a). On the other hand, for microporous catalysts no clear correlation was found, being a sign than for these materials, other factors, such as the pore size, should be considered. It is known that Fe<sup>3+</sup> is active in gasification of carbonaceous compounds [60] when it is reduced during oxidation of carbonaceous species. In addition, for FeNi/H-Beta-300 another reason for coking is metal particle sintering during the experiment (Table 2) promoting coking.

The temperature for the maximum heat release during TGA as a function of temperature is shown in Fig. 12b. For mesoporous catalysts the amount of coke increased with increasing temperature for the highest heat release. An analogous correlation was observed for the

**Fig. 9.** Normalized Fe K edge (left) and Ni K edge (right) XANES spectra of FeNi catalysts before and after TPR.

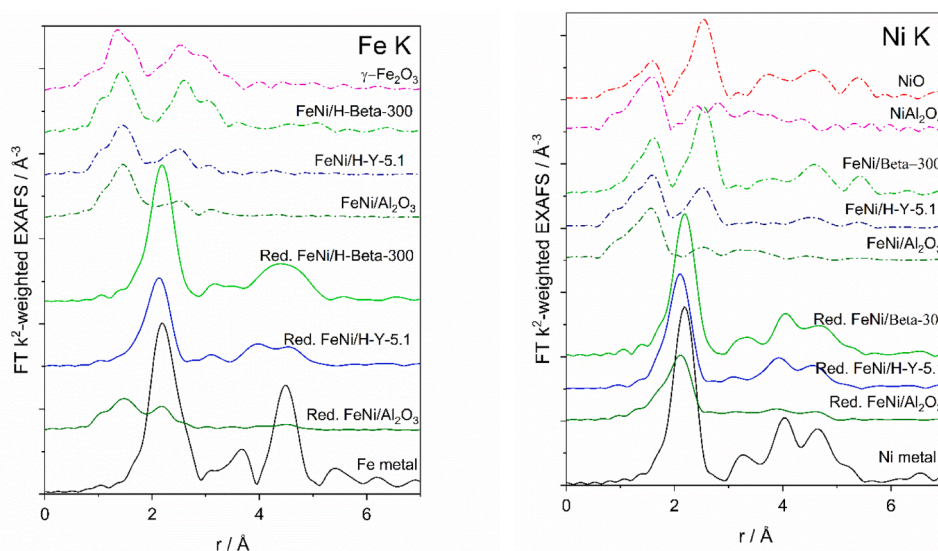


**Fig. 10.** Fourier transformed (FT)  $k^2$ -weighted Fe K edge (left) and Ni K edge (right) EXAFS spectra of FeNi catalysts before and after reduction. Distances are not corrected for the phase shift.

**Table 8**

A summary of Fe and Ni first shell coordination environments determined from the analysis of EXAFS spectra of reduced catalysts and reference metal foils. Note that due to similar X-ray atomic form factors of Fe and Ni these two elements are almost indistinguishable during EXAFS analysis, e.g. fully replacing Ni with Fe does not significantly change the fit statistics but decreases coordination number (CN) of the respective shell by approx. 10 %.

Sample / Edge	Fe foil	Ni foil	FeNi/H-Beta-300 Fe K	FeNi/H-Beta-300 Ni K	FeNi/H-Y-5.1 Fe K	FeNi/H-Y-5.1 Ni K	FeNi/Al <sub>2</sub> O <sub>3</sub> Fe K	FeNi/Al <sub>2</sub> O <sub>3</sub> Ni K
M-O distance (Å)	-	-	-	-	2.02 ± 0.02	-	1.94 ± 0.02	1.99 ± 0.02
CN (O)	-	-	-	-	1.1 ± 0.2	-	2.8 ± 0.3	1.9 ± 0.4
M-M distance (Å)	2.461 ± 0.006	2.491 ± 0.002	2.489 ± 0.007	2.491 ± 0.002	2.503 ± 0.004	2.492 ± 0.004	2.50 ± 0.01	2.49 ± 0.01
CN (M)*	8 6 $S_0^2 = 0.65 \pm 0.07$	12 $S_0^2 = 0.81 \pm 0.03$	10.8 ± 1.5	11.2 ± 0.5	8.1 ± 0.5	10.9 ± 0.6	2.1 ± 0.5	7.6 ± 1.0
$\sigma^2$ (10 <sup>-3</sup> Å <sup>2</sup> )	4.8 ± 0.7	6.9 ± 0.3	6.8 ± 1.1	6.9 ± 0.4	7.9 ± 0.5	7.9 ± 0.4	7.4 ± 1.8	9.2 ± 1.2
$\delta E_0$ (eV)	4.9 ± 1.2	6.2 ± 0.3	6.4 ± 1.1	5.1 ± 0.4	-6.0 ± 0.6	-8.1 ± 0.6	-3.2 ± 1.4	-8.5 ± 1.3

\* Only Ni nearest neighbours are used in the fits of FeNi catalysts (because of similarity in scattering functions of Fe and Ni).

**Table 9**

Comparison of detected phase with different methods. Notation: n.d. not determined.

Catalyst	EXAFS	XRD <sup>a</sup>	STEM-EDX <sup>b</sup>
FeNi/Al <sub>2</sub> O <sub>3</sub>	FeNi alloy, Fe-rich surface, NiAl <sub>2</sub> O <sub>4</sub>	FeNi alloy	FeNi alloy
FeNi/H-Y-5.1	Oxidized Fe species	Possible Fe <sub>0.9</sub> Ni <sub>0.1</sub>	n.d.
FeNi/Beta-300	alloy	No peaks for Fe or Ni	Monometallic or core shell like aggregates with nickel on outside, iron in core

<sup>a</sup> only spent catalysts were studied by XRD,

<sup>b</sup> fresh reduced catalysts

microporous catalysts. Based on CHNS analysis, the molar ratio of H/C was 1.9 for FeNi/Al<sub>2</sub>O<sub>3</sub> indicating the presence of nearly paraffinic type of coke [61], which might be easy to remove. This result is in accordance with XRD data showing no coke in spent FeNi/Al<sub>2</sub>O<sub>3</sub> catalyst. A high temperature of the maximum heat release was observed for FeNi/SiO<sub>2</sub> in line with a slightly higher coke content in the spent catalyst.

### 3.2. Catalytic results

The catalytic results showed that FeNi/Al<sub>2</sub>O<sub>3</sub> demonstrated the best performance in the hydrodeoxygenation (Table 11, Fig. 13). The highest initial TOF and conversion were also obtained with this catalyst. FeNi/Al<sub>2</sub>O<sub>3</sub> catalyst exhibited the smallest average metal particle size, the highest amount of surface metal sites (Table 2, Table 4) and the lowest

Brønsted to Lewis acid site ratio In [61] the highest initial TOF in guaiacol HDO at 230 °C under 40 bar with WHSV of 3.12 min<sup>-1</sup> was 0.18 s<sup>-1</sup> for FeNi/Beta zeolite with the metal particle size of 11.3 nm,

**Table 10**

TGA and CHNS results from the spent catalysts.

Catalyst	Coke (wt%)	T <sub>max</sub> (°C)	r <sub>coke</sub> (μgcoke/gcat/h)
FeNi/H-USY-30	4	338	6.7
FeNi/H-Y-5.1	7	349	11.7
FeNi/H-Beta-38	4	361	6.7
FeNi/H-Beta-300	10	380	16.7
FeNi/H-Al-MCM-48	2	339	3.3
FeNi/SiO <sub>2</sub>	5	317, 452	8.3
FeNi/Al <sub>2</sub> O <sub>3</sub>	1 (5.6 <sup>b</sup> )	331	1.7

<sup>a</sup> determined by CHNS analysis



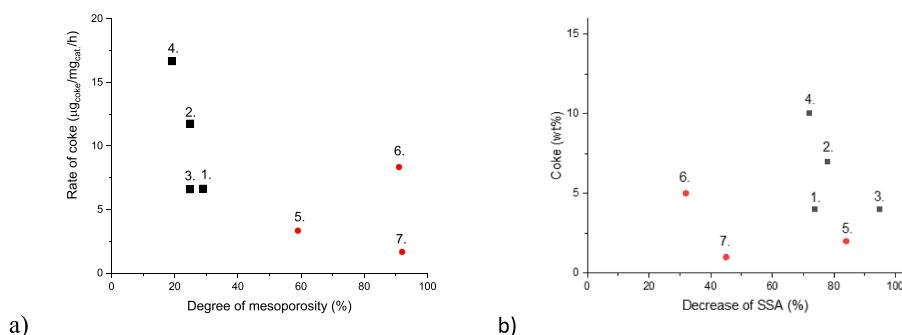


**Fig. 11.** a) The coking rate of the catalyst as a function of the degree of mesoporosity of the catalyst, b) the amount of coke as a function of the decrease of specific surface area (SSA) during TOS. Notation. Microporous catalysts (■): 1. FeNi/USY-30, 2. FeNi/H-Y-5.1, 3. FeNi/H-Beta-38, 4. FeNi/H-Beta-300, mesoporous catalysts (●): 5. FeNi/H-Al-MCM-48, 6. FeNi/SiO<sub>2</sub>, 7. FeNi/Al<sub>2</sub>O<sub>3</sub>.

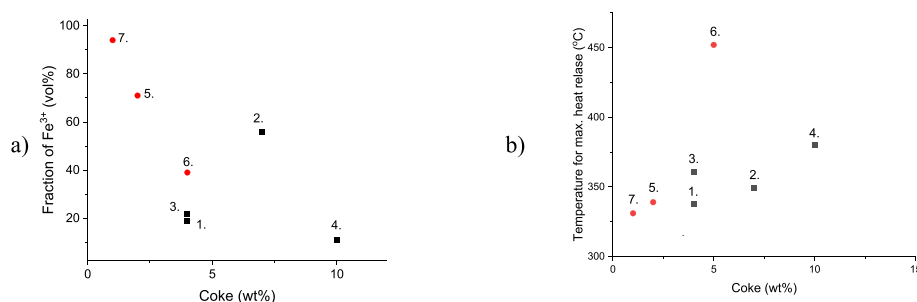


**Fig. 12.** a) Fraction of Fe<sup>3+</sup> species and b) temperature for the maximum heat release in TGA as a function of the amount of coke determined by TGA. Notation. Microporous catalysts (■): 1. FeNi/USY-30, 2. FeNi/H-Y-5.1, 3. FeNi/H-Beta-38, 4. FeNi/H-Beta-300, mesoporous catalysts (●): 5. FeNi/H-Al-MCM-48, 6. FeNi/SiO<sub>2</sub>, 7. FeNi/Al<sub>2</sub>O<sub>3</sub>.

while in the current case over FeNi/Al<sub>2</sub>O<sub>3</sub> (3.4 nm metal particle size) the corresponding value was 0.31 s<sup>-1</sup> for isoeugenol at 300 °C under 30 bar hydrogen. No direct correlation with the initial TOF and the average metal particle size or the Brønsted to Lewis acid site ratio could be established. This might be due to different properties of the supports, e.g. porosity. FeNi/USY-30 with its relatively large metal particles exhibited the second highest initial TOF. Analogously to FeNi/Al<sub>2</sub>O<sub>3</sub>, the mildly acidic FeNi/H-Beta-300 gave also a rather high initial TOF, while low TOFs were obtained with FeNi/H-Beta-38, FeNi/H-Al-MCM-48 and FeNi/SiO<sub>2</sub>.

After prolonged time-on-stream FeNi/Al<sub>2</sub>O<sub>3</sub> catalyst retained its high conversion, while the largest decrease for the DHE conversion was obtained over FeNi/SiO<sub>2</sub>, FeNi/H-Beta-300 and FeNi/H-Beta-38. The reason for the extensive deactivation of FeNi/SiO<sub>2</sub> and FeNi/H-Beta-300 catalysts is their prominent metal particle sintering. Superior stability of FeNi/Al<sub>2</sub>O<sub>3</sub> is also observed when comparing the deactivation rate with, for example, decline of the guaiacol conversion over NiFe on Beta zeolite catalyst being 1.2 %/min/g<sub>cat</sub> [62].

The products present in the reaction mixture are visible in the chromatogram in Fig. S13. The products have been grouped in oxygen-free cycloalkane derivatives, oxygen-free benzene and alkene derivatives, ethoxy-cycloalkanes, methoxy- and dipropylbenzenes, respectively. The calculated yields and selectivity to oxygen free compounds (OFC) over different catalysts confirm that FeNi/Al<sub>2</sub>O<sub>3</sub> is a superior catalyst (Fig. 13b,c). Over other catalysts DHE conversion decreased substantially with increasing TOS and, at the same time, selectivity to OFC products decreased for all other catalysts with decreasing conversion except for FeNi/Al<sub>2</sub>O<sub>3</sub> at 300 °C, however, oxygen containing propylphenol selectivity increased with increasing TOS for FeNi/Al<sub>2</sub>O<sub>3</sub> catalyst at 275 °C, when DHE conversion decreased (see section below). This catalyst exhibited the smallest metal particle size among the studied catalysts and has a very low Brønsted acidity (Table 4). A fair comparison of selectivity to OFC can be done for FeNi/H-Al-MCM-48 and FeNi/SiO<sub>2</sub>, which are both mesoporous. Higher selectivity to OFC products at 25 % DHE conversion of the former catalyst can be related to its smaller metal particle size in comparison to

**Table 11**

Catalytic results. Conditions: 300 °C, 30 bar hydrogen, WHSV 8.4 h<sup>-1</sup>, residence time for the liquid 8.4 min. 0.3 g catalyst, molar ratio of DHE:H<sub>2</sub> 1:15. Notation: dX denotes the decrease in DHE conversion during the first 15 min TOS. Notation: Values for selectivity given at DHE conversion X<sub>DHE</sub> = 25 %, in parenthesis values at 70 % DHE conversion.

Catalyst	X (%)	TOF (1/h)	dX (%/min)	S <sub>OFC</sub> (%)	S <sub>CHX</sub> (%)	S <sub>BENZD</sub> (%)	S <sub>PP</sub> (%)	S <sub>DMOXY</sub> (%)	Coke (wt%)
FeNi/USY-30	64	1178	0.22	n.a. (37)	n.a. (34)	n.a. (1)	n.a. (52)	n.a. (18)	3.6
FeNi/H-Y-5.1	67	899	0.10	n.a. (37)	n.a. (28)	n.a. (7)	n.a. (41)	n.a. (18)	7.69
FeNi/H-Beta-38	17	266	0.53	30 (n.a.)	29 (n.a.)	0.5 (n.a.)	60 (n.a.)	16 (n.a.)	3.6
FeNi/H-Beta-300	23	543	0.72	38 (72)	34 (63)	2 (5)	12 (17)	2 (4)	10.9
FeNi/Al-MCM-48	11	198	0.22	44 (n.a.)	38 (n.a.)	8 (n.a.)	42 (n.a.)	11 (n.a.)	2.0
FeNi/SiO <sub>2</sub>	13	238	1.0	19 (n.a.)	19 (n.a.)	94 (n.a.)	77 (n.a.)	0 (n.a.)	4.62
FeNi/Al <sub>2</sub> O <sub>3</sub>	100	1122	0	n.a. (100 <sup>a</sup> )	n.a. (95 <sup>a</sup> )	n.a. (2 <sup>a</sup> )	n.a. (0 <sup>a</sup> )	n.a. (0 <sup>a</sup> )	1.0

<sup>a</sup> X<sub>DHE</sub> = 100 %

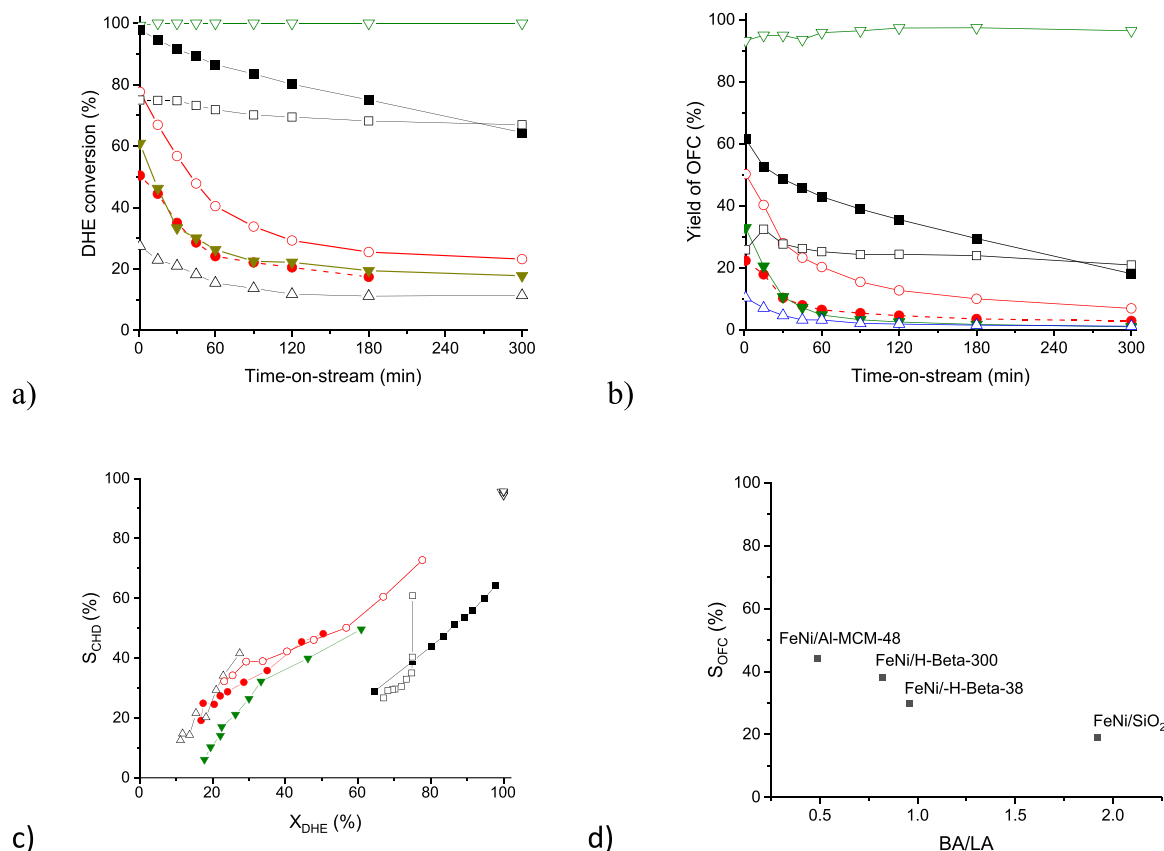


**Fig. 13.** a) DHE conversion, b) yield of oxygen free compounds c) Selectivity to oxygen free compounds (OFC) as a function of DHE conversion (notation: (▽) FeNi/Al<sub>2</sub>O<sub>3</sub>, (▼) FeNi/SiO<sub>2</sub>, (●) FeNi/H-Beta-38, (○) FeNi/H-Beta-300, (Δ) FeNi/H-Al-MCM-48, (■) FeNi/H-USY-30, (□) FeNi/H-Y-5.1) and d) selectivity to oxygen free compounds at 25 % conversion level of DHE over different catalyst as a function of Brønsted to Lewis acid site ratio (BA/LA). Conditions: 300 °C, 30 bar hydrogen, WHSV 8.4 h<sup>-1</sup>, residence time for the liquid 8.4 min. 0.3 g catalyst, molar ratio of DHE:H<sub>2</sub> 1:15.

that of FeNi/SiO<sub>2</sub> (Table 2). On the other hand, no clear correlation with OFC selectivity at 25 % conversion for FeNi/H-Beta-38, and FeNi/H-Beta-300 could be revealed.

An effort was made to correlate the selectivity to OFC products at 25 % and 70 % conversion levels with the Brønsted to Lewis acid site ratio (BA/LA) of the catalysts (Fig. 13d). Typically, selectivity to OFC decreased with the increasing BA/LA ratio at 25 % conversion level of DHE. This result indicates that Lewis acid sites (Table 2) are important for deoxygenation. However, at 75 % conversion level no clear correlation could be established and the best performing catalyst, FeNi/Al<sub>2</sub>O<sub>3</sub> with a low Brønsted to Lewis acid site ratio and a small average metal particle size exhibited complete conversion and selectivity under these conditions (Table 11).

Selectivity to different products as a function of DHE conversion over tested catalysts is shown in Fig. 14. DHE is primarily converted to propylphenols and 1,2-dimethoxy-4-n-propylbenzene (Fig. 14a, b). Propylphenol is formed via demethoxylation which occurs prior to dehydroxylation due to a higher bond energy in OH bound to aromatic ring (468 kJ/mol) in comparison to OR bound to aromatic ring (422 kJ/mol) [63]. Conversion of dihydroeugenol decreases with increasing time-on-stream and initially very low selectivity to 4-propylphenol was observed for FeNi/Al<sub>2</sub>O<sub>3</sub>. Very high selectivity to cyclohexyl products, in the range of 94–96 %, during the reaction was obtained over FeNi/Al<sub>2</sub>O<sub>3</sub> (Fig. 14d). Traces of ethoxy- and benzene derivatives were also visible. FeNi/Al<sub>2</sub>O<sub>3</sub> catalyzed also formation of benzene derivatives indicating that the consecutive reaction from 4-propylphenol to benzene derivatives was retarded due to catalyst deactivation. Selectivity to benzyl derivatives, is the highest for FeNi/H-MCM-48 (Fig. 14c), which exhibits large pores, while the metal particles are located mainly outside the pore structure. The benzene ring was not hydrogenated inside the

mesopores, however, deoxygenation occurred due to presence of medium strength Brønsted acid sites (Table 4). On the other hand, for other mesoporous catalysts, i.e. FeNi/SiO<sub>2</sub> and FeNi/Al<sub>2</sub>O<sub>3</sub> low selectivity to benzyl derivatives could be explained by much lower amounts of medium strength acid sites (Table 4). Selectivity to cyclohexyl products increased with increasing DHE conversion almost analogously for FeNi/Al-H-MCM-48, FeNi/H-Beta-300, and FeNi/H-Beta-38 (Fig. 14d), while slightly lower initial selectivity to these products was observed for FeNi/SiO<sub>2</sub> exhibiting also nearly no acidity and large metal particle sizes. On the other hand, FeNi/H-USY-30 and FeNi/H-Y-5.1 exhibited initially high conversion, but relatively low selectivity to cyclohexyl products. Especially high selectivity to oxygenated 1,2-dimethoxy-4-n-propylbenzene was obtained over FeNi/H-USY-30, which did not contain strong Brønsted acid sites (Table 4). Etherification of DHE forming 3,4-dimethylpropylbenzene catalyzed by the Brønsted acid sites [64] was the most prominent for FeNi/H-Beta-38, FeNi/H-Y-5.1, FeNi/USY-30 and FeNi/H-Al-MCM-48 (Fig. 12b). The latter catalyst exhibited large pores, while the three bimetallic zeolites had the highest amount of Brønsted acid sites (Table 4).

A detailed product distribution for the three most active catalysts is shown in Fig. 15. FeNi/Al<sub>2</sub>O<sub>3</sub> exhibited superior stability giving a nearly constant yield of the main product, propylcyclohexane, ranging from 84 % to 88 %. This catalyst demonstrated mild acidity, 3.4 nm metal particle size and a low hydrogen uptake. In addition, according to XANES, the catalyst contained FeNi alloy. The stable catalyst performance can be due to the presence of Ni-rich core surrounded by Fe located on the surface as observed by EXAFS and HRTEM. According to the literature [52], the highest cyclohexane yield in phenol HDO was obtained with NiFe supported on mesoporous carbon (MSC) at 250 °C under 50 bar. This catalyst with 4.5 nm metal crystallites contained

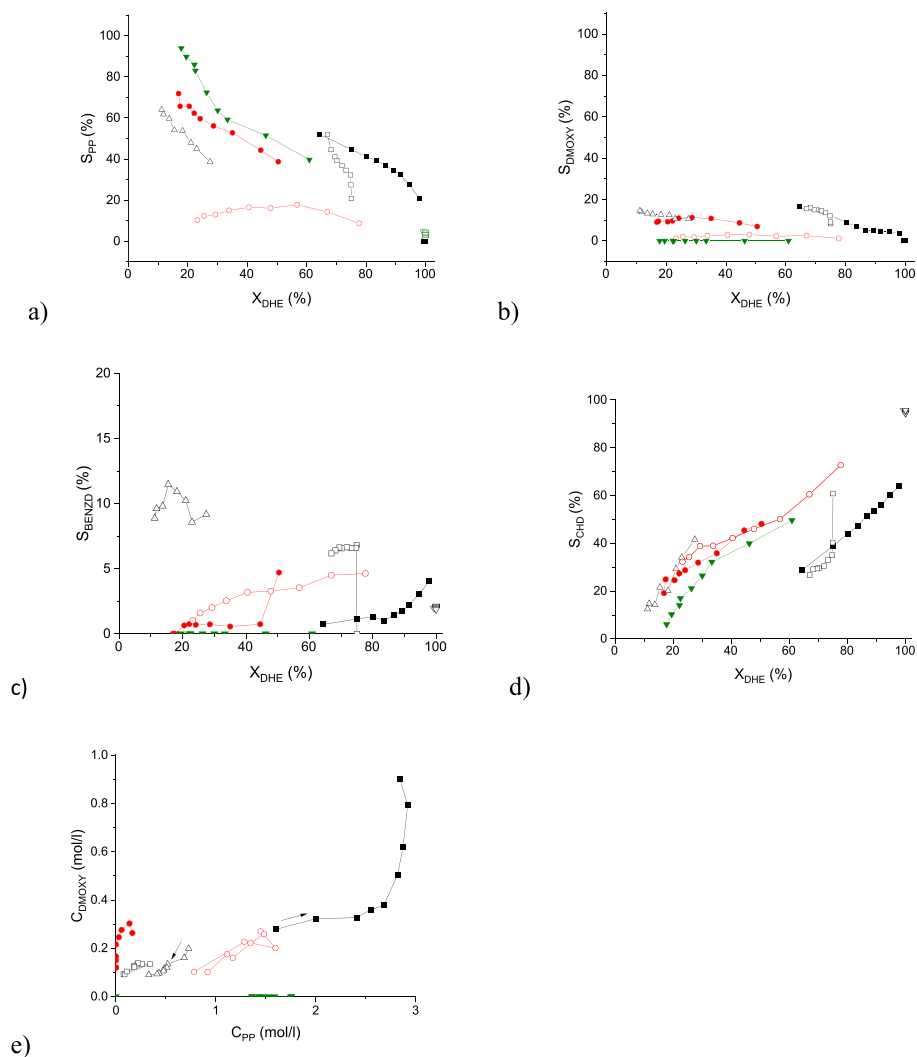


**Fig. 14.** Selectivity to a) 4-propylphenol (PP), b) 1,2-dimethoxy-4-n-propylbenzene (DMOXY), c) propylbenzene (PB) and d) cyclohexyl derivatives (CHD), as a function of DHE conversion over different catalysts and e) concentration of 1,2-dimethoxy-4-n-propylbenzene vs concentration of 4-propylphenol. Conditions: 300 °C, 30 bar hydrogen, WHSV 8.4 h<sup>-1</sup>, residence time for the liquid 8.4 min. 0.3 g catalyst, molar ratio of DHE:H<sub>2</sub> 1:15. Notation (▽) FeNi/Al<sub>2</sub>O<sub>3</sub>, (▼) FeNi/SiO<sub>2</sub>, (●) FeNi/H-Beta-38, (○) FeNi/H-Beta-300, (Δ) FeNi/H-Al-MCM-48, (■) FeNi/H-USY-30 and (□) FeNi/H-Y-5.1.

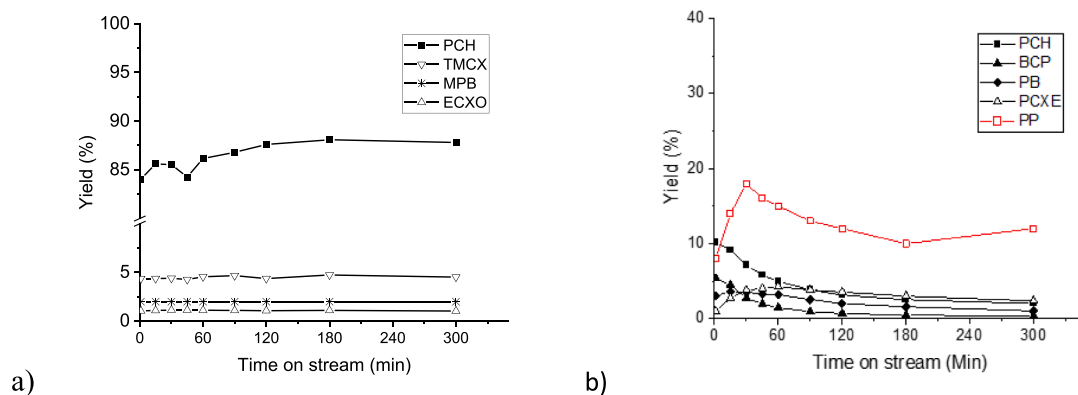


**Fig. 15.** The yield of the main products in HDO of DHE over a) FeNi/Al<sub>2</sub>O<sub>3</sub>, b) FeNi/H-Beta-300. Notation: 4-propylcyclohexane (PCH), butenylcyclopentane (BCP), 1-propylcyclohexene (PCXE), 1,3,5-trimethylcyclohexane (TMCX), propylbenzene (PB), 4-propylphenol (PP), 1-methyl-2-propylbenzene (MPB), PCXE propylcyclohexene (PCXE), 2-ethoxy-2-cyclohexen-1-one (ECXO). Conditions: 300 °C, 30 bar hydrogen, WHSV 8.4 h<sup>-1</sup>, residence time for liquid 8.4 min. 0.3 g catalyst, molar ratio of DHE:H<sub>2</sub> 1:15.

Fe<sub>1</sub>Ni<sub>3</sub> alloy as confirmed by XRD. The hydrogen uptake of NiFe/MSO was rather low. It was furthermore stated that a too high hydrogen coverage might inhibit cyclohexanol adsorption due to the spillover of dissociated H close to Ni-Fe sites [53]. The role of Fe in a bimetallic catalyst is to adsorb reactants through hydroxyl species, while hydrogen activation occurs on the Ni sites. Thus, synergy between Ni and Fe promotes hydrodeoxygenation of phenolic compounds.

The second-best catalyst, FeNi/H-Beta-300, was giving initially only ca. 10 % propylcyclohexane (Fig. 15b). It exhibited much smaller HDO activity compared to FeNi/Al<sub>2</sub>O<sub>3</sub> due to its large metal particles (Table 2) and the main product was 4-propylphenol (Fig. 15 b).

Over FeNi/H-Beta-300 also ring contraction occurred and the ratio between the yield of propylcyclohexane to butenylcyclopentane increased from the initial value of 2–5.8 at time-on-stream of 180 min, while thereafter it decreased to 3.8 at TOS= 300 min. As a comparison, no ring contradiction occurred over FeNi/Al<sub>2</sub>O<sub>3</sub> due to presence of only mild Brønsted acid sites. It is known that ring contraction of the six-member ring hydrocarbon compounds occurs for example at 400 °C over a mixture of Pt/SiO<sub>2</sub> and H-ZSM-5 [65] and ring contracting mechanism over metals are reviewed in [66]. Ethylcyclohexane was isomerized to several products, among which was isopropylcyclopentane over Ni supported on silica-alumina at 286 °C [67]. Furthermore, methylcyclohexane reacted to aromatics as the main products, and the second most prominent products were isomerization ones, e.g. ethylcyclopentane and 1,2-dimethylcyclopentane over P<sub>2</sub>O<sub>5</sub> modified 17 wt% NiO-1.4 wt% Fe/ZSM-5 at 400 °C [68]. The mechanism for hydrocracking/isomerization of methylcyclohexane is as follows. Initial transformation of methyl cyclohexane starts with dehydrogenation on the metal sites followed by protonation of the formed olefin on the Brønsted acid sites to the corresponding carbenium ions. In the subsequent step the formed ions isomerize followed by hydrogenation of ethylcyclopentane [68].

For the best catalyst FeNi/Al<sub>2</sub>O<sub>3</sub>, the experiments were also performed at 275 °C, because conversion at 300 °C for this catalyst was 100 % during the whole reaction not allowing proper evaluation of the catalyst activity and stability. The initial conversion of DHE was 65 % decreasing during 6 h TOS to 10 %. Deoxygenation efficiency was much lower at 275 °C in comparison to 300 °C because in the former case the yield of oxygen free compounds was initially 60 declining to 37 % with increasing time-on-stream. The main products initially were 2-ethoxy-2-cyclohexene-1-one and propylphenol, while the yields of oxygen-free products, such as propylcyclohexene decreased rapidly with increasing time-on-stream.

### 3.3. Theoretical studies

**Adsorption.** Initially, adsorption of the model isoeugenol was studied. This compound is quickly hydrogenated to dihydroeugenol, and its

hydrogenation was compared to those of long-chain *n*-hydrocarbons, which compete in the production of fuels from renewables. Adsorption energies of saturated hydrocarbons with metallic surfaces are dominated by the dispersion interactions, which scale linearly with the molecule size. As shown in Fig. 16, each -CH<sub>2</sub>- increases the interaction for 0.19 eV, 0.16 eV, 0.14 eV and 0.13 eV on Ni(111), FeNi<sub>3</sub>(111), FeNi(110) and Fe(110), respectively, allowing to extrapolate to larger hydrocarbons. On the other hand, isoeugenol exhibits an adsorption energy of −2.85, −2.47, −2.48 and 2.82 eV on Ni(111), FeNi<sub>3</sub>(111), FeNi(110) and Fe(110), respectively, since other van der Waals forces can also contribute. This means that on Ni-rich catalysts, isoeugenol binds as strongly as C<sub>15</sub>H<sub>32</sub>, while on Fe(110) this equivalence is shifted towards C<sub>22</sub>H<sub>46</sub>. For the catalyst to perform well for dihydroeugenol transformations, the amount of larger hydrocarbons should be minimized. Secondly, it was observed that Ni-rich catalysts bind saturated hydrocarbons relatively more strongly than Fe-rich catalysts, which is not the case for isoeugenol. Thus, from the computational experience it is important to use FeNi as opposed to pure Ni to prevent catalyst poisoning.

**Reaction mechanism.** To decouple the individual contributions of Fe and Ni, further calculations were performed on pure Ni(111) and Fe(110) because based on the characterization data instead of an ideal alloy, metal particles with non-uniform contribution are formed. Thus, the model can treat Ni and Fe separately.

While the reaction mechanism consists of several elementary steps, they can be lumped in the following transformations: (i) hydrogenation of isoeugenol to dihydroeugenol (C=C hydrogenation), (ii) hydrodeoxygenation of the methoxy group / demethoxylation (removal of -OCH<sub>3</sub>), (iii) reduction of the hydroxyl group / dehydroxylation (removal of -OH) and (iv) ring saturation (hydrogenation of the aromatic core). Skeletal isomerization along with degradation reactions were not modelled.

To keep the number of combinatorial possibilities manageable, each transformation was sequentially treated, not accounting for the alternative mechanisms. For instance, upon the cleavage of the C-H bond in the -OCH<sub>3</sub> group, the methoxy group is considered to be hydrotreated to completion before the ring or the hydroxyl group would react. This is justified since the system follows the lowest energy pathway, while the transient formation of unstable intermediates generally increases the energy.

All hydrogenation reactions depend on the availability of active hydrogen species H\*, which is formed by the dissociative adsorption of H<sub>2</sub> on the catalyst. On Ni(111), H<sub>2</sub> physisorbs with an interaction of −0.42 eV and dissociates upon overcoming a small barrier of 2.4 kcal mol<sup>−1</sup>. On Fe(110), H<sub>2</sub> does not interact with the surface but readily transforms to H\* with a negligible barrier. The adsorption energy of H\* (relative to ½ H<sub>2</sub>) is −1.46 eV on Fe(110) and −0.59 eV on Ni(111).

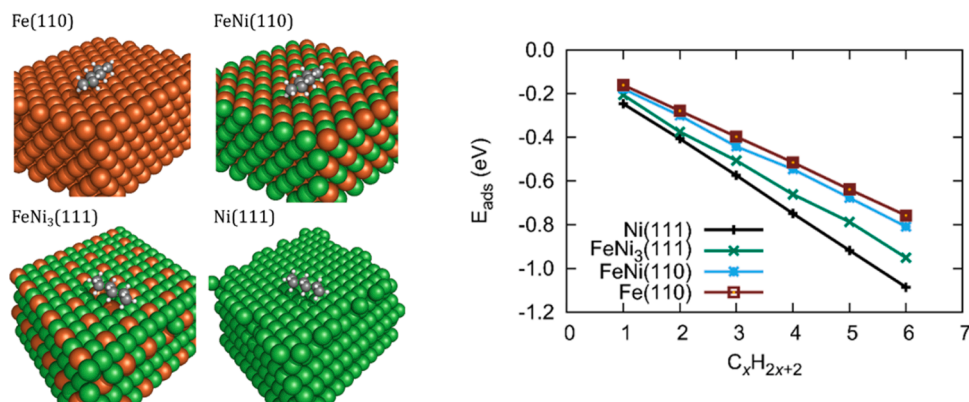


Fig. 16. Adsorption energies of saturated hydrocarbons linearly increase with the length of the carbon backbone.



Hydrogenation of isoeugenol to dihydroeugenol consists of two elementary steps proceeding faster on Ni. While the reactions are slightly endothermic, the barriers are 14.1 and 11.5 kcal mol<sup>-1</sup> on Ni and 13.4 eV and 20.9 kcal mol<sup>-1</sup> on Fe. Next, the methoxyl group is cleaved away in a step-wise fashion. Initially, all three C-H bonds are broken with activation barriers of 16.7, 10.4 and 14.7 kcal mol<sup>-1</sup> on Ni and 16.4, 3.7 and 6.1 kcal mol<sup>-1</sup> on Fe. The resulting PhO-C\* species then loses CO in one step with barriers of 11.4 and 9.8 kcal mol<sup>-1</sup>. The alternative route, where C\* and O\* were cleaved away sequentially is kinetically inaccessible, although thermodynamically more favourable. Lastly, one H\* is used to restore the aromaticity of the core in a fast step.

It is much more costly to hydrogenate phenol to benzene. While the cleavage of the PhO-H bond readily proceeds, especially on acidic catalysts, Ph-O bond is extremely difficult to dissociate (barriers of 36.1 and 27.4 kcal mol<sup>-1</sup> on Ni and Fe, respectively). Instead, the hydroxyl group is cleaved away as OH\* (barriers of 34.6 and 22.3 kcal mol<sup>-1</sup> on Ni and Fe, respectively) (Table 12), which quickly reacts with available H\* to form H<sub>2</sub>O. Finally, the ring is saturated step-by-step. The barriers on Ni range from 9.4 to 21.1 kcal mol<sup>-1</sup> and from 10.4 to 31.9 kcal mol<sup>-1</sup> on Fe. The detailed mechanism is shown in Fig. 17 while geometries of the transition states of the rate-determining steps (RDS) are shown in Fig. 18.

Several conclusions can be drawn from these values, in particular why both Ni and Fe are required in efficient catalysts. The availability of active hydrogen is higher on Fe and competing unsaturated hydrocarbons are less strongly bound. On the other hand, Fe is a poorer hydrogenation catalyst precisely due to the strong adsorption of hydrogen. The hydrogenation of isoeugenol on Fe is substantially slower and more endothermic than on Ni. Similarly, the ring hydrogenation is slower on Fe and strongly endothermic. Neat Ni, however, is also not efficient. The deoxygenation reactions have lower barriers and more negative energy change on Fe than on Ni. FeNi catalysts can therefore benefit from existence of the most appropriate metal for each individual transformation. Furthermore, modifying the ratio between Ni and Fe could help to steer the reaction towards the desired products.

#### 4. Conclusions

Several different iron-nickel supported catalysts were prepared in this work using a two step impregnation method. The catalysts were comprehensively characterized by different physico-chemical methods and tested in solventless continuous hydrodeoxygenation of dihydroeugenol. The novelty in the work is in revealing the active catalytic species for HDO, such as formation of the alloy and the nature of the

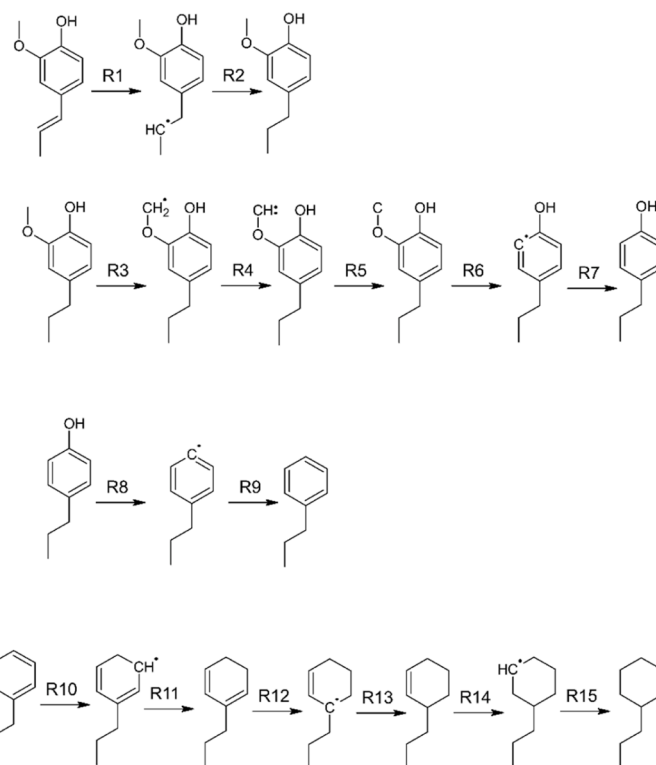


Fig. 17. The elementary reaction mechanism for hydrodeoxygenation of isoeugenol (and dihydroeugenol) on FeNi catalysts.

local environment of the metal using advanced methods including EXAFS-XANES and STEM-EDX. In addition, the reaction mechanism was proposed using quantum chemical calculations.

The results revealed that the best catalytic performance in dihydroeugenol hydrodeoxygenation was obtained over FeNi/Al<sub>2</sub>O<sub>3</sub> at 300 °C under 30 bar hydrogen with the weight hour space velocity of 8.4 h<sup>-1</sup> resulting in complete conversion of dihydroeugenol and the yields of the main product propylcyclohexane in the range of 84–88 %. This catalyst exhibited mild acidity, 3.4 nm metal particles of the size 3.4 nm with well dispersed nickel and iron on Al<sub>2</sub>O<sub>3</sub> support. Furthermore, FeNi/Al<sub>2</sub>O<sub>3</sub> contained FeNi alloy particles with the fcc metallic structure based on XANES spectra. The performance of FeNi/Al<sub>2</sub>O<sub>3</sub> was very stable during 5 hours time-on-stream due to the presence of Ni-rich particles with iron located on the outer surface, based on EXAFS measurements. When comparing the performance of FeNi/Al<sub>2</sub>O<sub>3</sub> catalyst to other investigated materials, it should be that only the former one gave a stable complete conversion and 100 % selectivity to deoxygenated products during 300 min time-on-stream under the studied conditions, while the others catalysts deactivated with increasing time-on-stream. The best FeNi/Al<sub>2</sub>O<sub>3</sub> catalyst exhibited the smallest average metal particle size and the lowest Brønsted to Lewis acid site ratio in comparison to other catalysts.

Theoretical calculations showed the importance of using FeNi catalysts as opposed to solely Fe or Ni. While Fe is superior for deoxygenation reactions, Ni performs better for hydrogenation. Furthermore, Ni moderates hydrogen adsorption, which is too strong on Fe.

While the paper was focusing on utilization of one model compound, dihydroeugenol, in eventual industrial settings a mixture of phenolic compounds will be used and the impurities present in the feed can influence the catalytic behavior. The future work will address these important aspects of HDO of lignin phenolics.

Table 12

Activation barriers and reaction energies for individual reaction steps (see Fig. 17) of isoeugenol (and dihydroeugenol) hydrodeoxygenation on Ni(111) and Fe(110). All values are reported in kcal mol<sup>-1</sup>.

Reaction	Ni(111)		Fe(110)	
	<i>E<sub>a</sub></i>	Δ <i>E</i>	<i>E<sub>a</sub></i>	Δ <i>E</i>
R1	14.1	+ 3.4	13.4	+ 9.6
R2	11.4	+ 4.0	20.9	+ 9.0
R3	16.7	+ 3.5	16.4	-2.9
R4	10.4	-1.9	3.7	-7.2
R5	14.7	-2.8	6.1	-14.8
R6	11.4	-24.0	9.8	-25.4
R7	11.2	-14.4	13.9	-7.9
R8	34.6	+ 7.8	22.3	-12.8
R9	9.6	-19.5	13.4	-10.5
R10	20.8	+ 13.6	31.9	19.5
R11	13.6	+ 11.4	10.4	+ 7.1
R12	21.1	+ 2.5	15.0	+ 12.2
R13	9.4	-0.9	17.4	+ 10.5
R14	15.9	+ 5.6	16.4	+ 14.9
R15	13.5	-7.1	22.7	+ 0.0

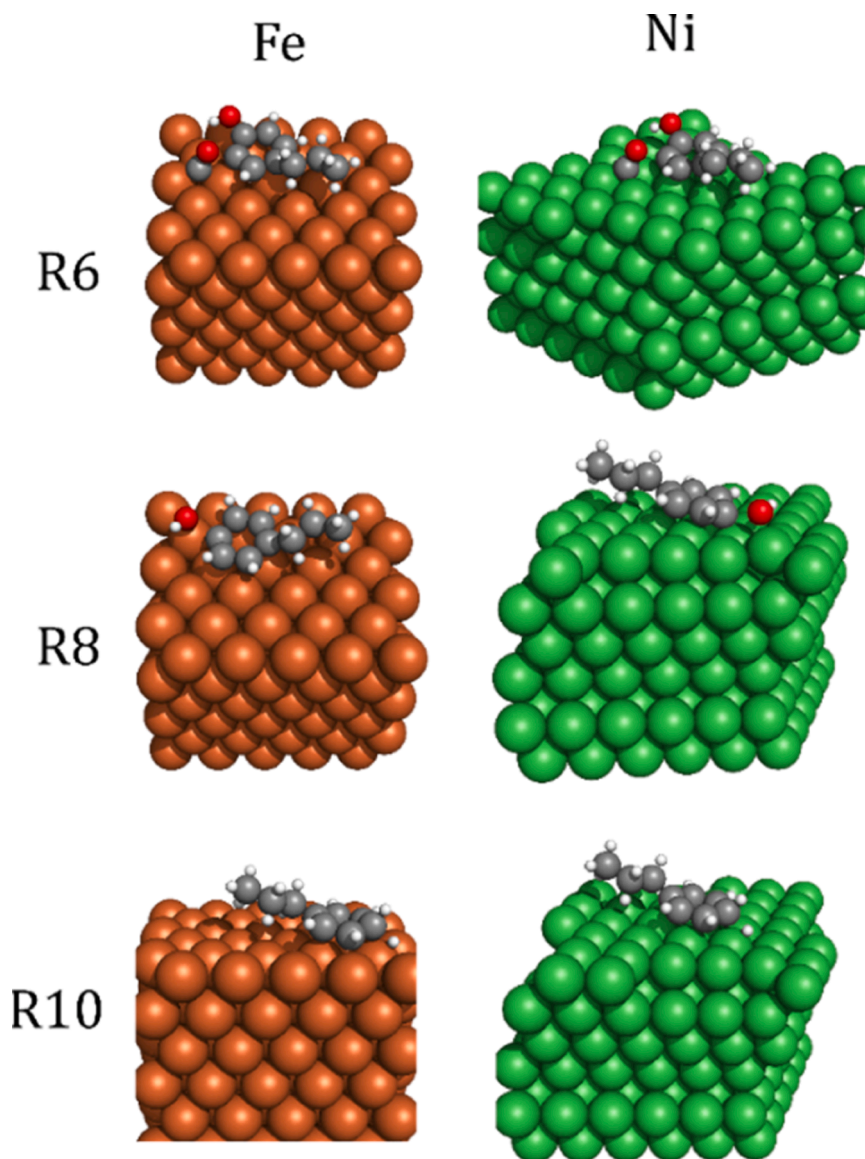


Fig. 18. Transition states of the rate-determining steps for the three transformations (demethoxylation, dehydroxylation, ring saturation).

#### CRedit authorship contribution statement

**Huš Matej:** Investigation. **Likožar Blaž:** Methodology, Investigation. **Lastusaari Mika:** Investigation. **Vajglová Zuzana:** Investigation. **Lindén Johan:** Investigation. **Mäki-Arvela Päivi:** Writing – original draft, Supervision, Methodology, Investigation. **Doronkin Dmitry E.:** Investigation. **Yevdokimova Olha:** Investigation. **Murzin Dmitry Yu.:** Writing – review & editing, Supervision, Project administration, Methodology, Funding acquisition, Conceptualization. **Martinez-Klimov Mark:** Investigation. **Simakova Irina:** Investigation. **Eränen Kari:** Resources, Project administration, Formal analysis. **Tirri Teija:** Methodology, Investigation. **van Hoeven Jessi E. S.:** Investigation. **Peuronen Anssi:** Writing – original draft, Investigation.

#### Declaration of Competing Interest

The authors declare that they have no known competing financial interests or personal relationships that could have appeared to influence the work reported in this paper.

#### Acknowledgement

The authors acknowledge Business Finland for funding through the project: Catalytic Slurry Hydrotreatment. Electron microscopy samples were processed and analyzed at the Electron Microscopy Laboratory, Institute of Biomedicine, University of Turku, which received financial support from Biocenter Finland. We acknowledge DESY (Hamburg, Germany), a member of the Helmholtz Association HGF, for the provision of experimental facilities. Parts of this research were carried out at the light source PETRA III at DESY, a member of the Helmholtz Association (HGF). We would like to thank Dr. Edmund Welter for his assistance in using the beamline P65, which was allocated for proposal I-20220246. Computational resources were provided by the Institute of Information Science, Maribor, Slovenia through the HPC RIVR consortium and EuroHPC JU. Financial support from the Slovenian Research and Innovation Agency (ARIS) through core funding P2-0152, project funding N2-0316, J1-3020 and infrastructure funding I0-0039 is greatly appreciated.

## Appendix A. Supporting information

Supplementary data associated with this article can be found in the online version at [doi:10.1016/j.apcata.2025.120307](https://doi.org/10.1016/j.apcata.2025.120307).

## Data availability

Data will be made available on request.

## References

- [1] C.-H. Zhou, X. Xia, C.-X. Lin, D.-S. Tong, J. Beltramini, Catalytic conversion of lignocellulosic biomass to fine chemicals and fuels, *Chem. Soc. Rev.* 40 (11) (2011) 5588–5617.
- [2] A.G. Kedia, P. Kumar, A. Dutta, Value added hydrocarbons from lignin derived bio-oils: Insights from process simulations, *Mat. Today.: Proc.* 72 (2023) 187–191.
- [3] A.A. Dwiatiemo, J. Seo, J.W. Choi, D.J. Suh, J. Jae, J.M. Ha, Improved activity of a CaCO<sub>3</sub>-supported Ru catalyst for the hydrodeoxygenation of eugenol as a model lignin-derived phenolic compound, *Catal. Commun.* 127 (2019) 45–50, 127.
- [4] M. Zhao, J. Hu, P. Lu, S. Wu, C. Liu, Y. Sun, Efficient hydrodeoxygenation of lignin-derived bio-oil to hydrocarbon fuels over bifunctional RuCoWx/NC catalysts, *Fuel* 326 (2022) 125020.
- [5] M.E. Martínez-Klimov, P. Mäki-Arvela, Z. Vajglova, M. Alda-Onggar, I. Angervo, N. Kumar, K. Eränen, M. Peurla, M.H.A. Calimili, I.L. Shchukarev, I.L. Simikova, D. Yu. Murzin, Hydrodeoxygenation of isoeugenol over carbon-supported Pt and Pt–Re catalysts for production of renewable jet fuel, *Energy Fuels* 35 (21) (2021) 17755–17768.
- [6] M. Alda-Onggar, P. Mäki-Arvela, K. Eränen, A. Aho, J. Hemming, P. Paturi, M. Peurla, M. Lindblad, I.L. Simikova, D. Yu. Murzin, Hydrodeoxygenation of isoeugenol over alumina-supported Ir, Pt, and Re catalysts, *ACS Sust. Chem. Eng.* 6 (12) (2018) 16205–16218.
- [7] C. Lindfors, P. Mäki-Arvela, P. Paturi, A. Aho, K. Eränen, J. Hemming, M. Peurla, D. Kubická, I.L. Simakova, D. Yu. Murzin, Hydrodeoxygenation of isoeugenol over Ni- and Co-supported catalysts, *ACS Sust. Chem. Eng.* 7 (17) (2019) 14545–14560.
- [8] S. Tieuli, P. Mäki-Arvela, M. Peurla, K. Eränen, J. Wärnå, G. Cruciani, F. Menegazzo, D. Murzin, M. Signoretti, Hydrodeoxygenation of isoeugenol over Ni-SBA-15: kinetics and modelling, *Appl. Catal. A: Gen.* 580 (2019) 1–10.
- [9] A. Bjelić, M. Grilc, B. Likozar, Bifunctional metallic-acidic mechanisms of hydrodeoxygenation of eugenol as lignin model compound over supported Cu, Ni, Pd, Pt, Rh and Ru catalyst material, *Chem. Eng. J.* 394 (2020) 124914.
- [10] X. Yue, S. Zhang, N. Shang, S. Gao, Z. Wang, C. Wang, Porous organic polymer supported PdAg bimetallic catalyst for the hydrodeoxygenation of lignin-derived species, *Ren. Energy* 149 (2020) 600–608, 149.
- [11] D. Raikwar, S. Majumdar, D. Shee, Synergistic effect of Ni-Co alloying on hydrodeoxygenation of guaiacol over Ni-Co/Al<sub>2</sub>O<sub>3</sub> catalysts, *Mol. Catal.* 499 (2021) 111290.
- [12] B.S. Li, B.X. Feng, K.Y. Wu, T.H. Yang, Hydrodeoxygenation of lignin derived bio-oil into aromatic hydrocarbons over Ni-Cu-Ru/HZSM-5 catalyst, *J. Fuel Chem. Technol.* 51 (3) (2023) 358–365, 51(3).
- [13] X. Dou, W. Li, C. Zhu, X. Jiang, Catalytic waste Kraft lignin hydrodeoxygenation to liquid fuels over a hollow Ni-Fe catalyst, *Appl. Catal. B: Env.* 287 (2021) 119975.
- [14] X. Yue, L. Zhang, L. Sun, S. Gao, W. Gao, X. Cheng, N. Shang, Y. Gao, C. Wang, Highly efficient hydrodeoxygenation of lignin-derivatives over Ni-based catalyst, *Appl. Catal. B: Env.* 293 (2021) 120243.
- [15] N.K.G. Silva, R.A. Ferreira, R.M. Ribas, R.S. Monteiro, M.A.S. Barrozo, R.R. Soares, R.R. Gas-phase hydrodeoxygenation (HDO) of guaiacol over Pt/Al<sub>2</sub>O<sub>3</sub> catalyst promoted by Nb<sub>2</sub>O<sub>5</sub>, *Fuel* 287 (2021) 119509.
- [16] T.U.O. Jie, S.Q. Li, X.U. Hao, Y.J. Guan, W.U. Peng, Research progress of structure design and acidity tuning of zeolites for the catalytic conversion of syngas, *J. Fuel Chem. Technol.* 51 (1) (2023) 1–17.
- [17] R.K. Mishra, S.M. Chistie, S.U. Naika, K. Mohanty, Catalytic pyrolysis of biomass over zeolites for bio-oil and chemical production: a review on their structure, porosity, acidity co-relation, *Biores. Technol.* (2022) 128189.
- [18] H. Shafaghath, P.S. Rezaei, W.M.A.W. Daud, Catalytic hydrodeoxygenation of simulated phenolic bio-oil to cycloalkanes and aromatic hydrocarbons over bifunctional metal/acid catalysts of Ni/HBeta, Fe/HBeta and NiFe/HBeta, *J. Ind. Eng. Chem.* 35 (2016) 268–276.
- [19] M. Bregolato, V. Bolis, C. Busco, P. Ugliengo, S. Bordiga, F. Cavani, N. Ballarini, L. Maselli, S. Passeri, I. Rossetti, L. Forni, Methylation of phenol over high-silica beta zeolite: effect of zeolite acidity and crystal size on catalyst behaviour, *J. Catal.* 245 (2) (2007) 285–300.
- [20] H. Ma, H.W. Zhang, D. Chen, Catalytic hydrodeoxygenation of phenolic compounds over Ru-MoFeP/Al<sub>2</sub>O<sub>3</sub> catalyst, *Catal. Today* 408 (2023) 50–57.
- [21] K. Li, R. Wang, J. Chen, Hydrodeoxygenation of anisole over silica-supported Ni<sub>2</sub>P, MoP, and NiMoP catalysts, *Energy Fuels* 25 (3) (2011) 854–863.
- [22] S. Cheng, L. Wei, J. Julson, M. Rabnawaz, Upgrading pyrolysis bio-oil through hydrodeoxygenation (HDO) using non-sulfided Fe-Co/SiO<sub>2</sub> catalyst, *Energy Conv. Manag.* 150 (2017) 331–342.
- [23] M. Guisnet, P. Magnoux, Coking and deactivation of zeolites: influence of the pore structure, *Appl. Catal.* 54 (1) (1989) 1–27.
- [24] P.C. Shih, H.P. Lin, C.Y. Mou, Ultrastable acidic MCM-48-S assembled from zeolite seeds, *Stud. Surf. Sci. Catal.* 146 (2003) 557–560.
- [25] B.T. Kusema, L. Faba, N. Kumar, P. Mäki-Arvela, E. Díaz, S. Ordóñez, T. Salmi, D. Yu. Murzin, Hydrolytic hydrogenation of hemicellulose over metal modified mesoporous catalyst, *Catal. Today* 196 (1) (2012) 26–33.
- [26] M. Käldestrom, N. Kumar, T. Heikkilä, M. Tiitta, T. Salmi, D.Yu. Murzin, Formation of furfural in catalytic transformation of levoglucosan over mesoporous materials, *ChemCatChem* 2 (5) (2010) 539–546.
- [27] Z. Vajglová, O. Yevdokimova, A. Medina, K. Eränen, T. Tirri, J. Hemming, J. Linden, I. Angervo, P. Damlin, D. Doronkin, P. Mäki-Arvela, D.Yu. Murzin, Solventless hydrodeoxygenation of isoeugenol and dihydroeugenol in batch and continuous modes over a zeolite-supported FeNi catalyst, *Sus. Energy Fuels* 7 (18) (2023) 4486–4504.
- [28] I.L. Simakova, Y.S. Demidova, M.N. Simonov, P.S. Nipadkar, V.V. Bokade, V. V. Devi N, P.L. Dhepe, D.Y. Murzin, Mesoporous carbon and microporous zeolite supported Ru catalysts for selective levulinic acid hydrogenation into  $\gamma$ -valerolactone, *Catal. Sust. Energy* 6 (2019) 38–49.
- [29] I. Simakova, P. Mäki-Arvela, M. Martínez-Klimov, J. Müller, Z. Vajglova, M. Peurla, K. Eränen, D. Yu. Murzin, Continuous synthesis of menthol from citronellal and citral over Ni-Beta-zeolite-sepiolite composite catalyst, *Appl. Catal. A: Gen.* 636 (2022) 1–11, 11858 6.
- [30] T. Degen, M. Sadki, E. Bron, U. König, G. Nénert, The HighScore suite, *Powder Diff.* 29 (ement S2) (2014) S13–S18.
- [31] S. Gates-Rector, T. Blanton, The Powder Diffraction File: a quality materials characterization database, *Powder Diff.* 34 (2019) 352–360.
- [32] C.A. Emeis, Determination of integrated molar extinction coefficients for infrared absorption bands of pyridine adsorbed on solid acid catalysts, *J. Catal.* 141 (2) (1993) 347–354.
- [33] B. Ravel, M. Newville ATHENA, ARTEMIS, HEPHAESTUS: data analysis for X-ray absorption spectroscopy using IFEFFIT, *J. Synchrotron Rad.* 12 (2005) 537–541..
- [34] Z. Vajglova, N. Kumar, P. Mäki-Arvela, K. Eränen, M. Peurla, L. Hupa, M. Nurmi, M. Toivakka, D. Yu. Murzin, Synthesis and physicochemical characterization of shaped catalysts of  $\beta$  and Y zeolites for cyclization of citronellal, *Ind. Eng. Chem. Res.* 58 (39) (2019) 18084–18096.
- [35] I.L. Simakova, P. Mäki-Arvela, M. Martínez-Klimov, J. Müller, Z. Vajglova, M. Peurla, K. Eränen, D.Yu. Murzin, One-pot synthesis of menthol starting from citral over Ni supported on attapulgite-H-Beta-38 extrudates in a continuous flow: effect of metal location, *Ind. Eng. Chem. Res.* 61 (35) (2022) 12998–13010.
- [36] Z. Vajglová, N. Kumar, M. Peurla, J. Peltonen, I. Heinmaa, D.Yu. Murzin, Synthesis and physicochemical characterization of beta zeolite–bentonite composite materials for shaped catalysts, *Catal. Sci. Technol.* 8 (23) (2018) 6150–6162.
- [37] H. Silva, M.G. Nielsen, E.M. Fiordaliso, C.D. Damsgaard, C. Gundlach, T. Kasama, I. Chorkendorff, D. Chakraborty, Synthesis and characterization of Fe–Ni/γ-Al<sub>2</sub>O<sub>3</sub> egg-shell catalyst for H<sub>2</sub> generation by ammonia decomposition, *Appl. Catal. A: Gen.* 505 (2015) 548–556.
- [38] M. Przydacz, M. Jędrzejczyk, J. Rogowski, D. Ihiwakrim, N. Keller, A.M. Ruppert, TiO<sub>2</sub> supported non-noble Ni-Fe catalysts for the high yield production of 2,5-dimethylfuran biofuel, *Fuel* 356 (2024) 129606.
- [39] T. Ye, Y. Bai, K. Wang, W. Hu, M. Zhang, L.M. Wu, A route to selectively increase the microporous structure of zeolite and its optimization in the ethanol to butadiene reaction, *Ind. Chem. Mat.* 2 (1) (2024) 100–109.
- [40] R. Sabarish, G. Unnikrishnan, A novel anionic surfactant as template for the development of hierarchical ZSM-5 zeolite and its catalytic performance, *J. Por. Mat.* 27 (2020) 691–700.
- [41] R. Schmidt, M. Stöcker, D. Akporiaye, E.H. Tørstad, A. Olsen, High-resolution electron microscopy and X-ray diffraction studies of MCM-48, *Micro Mat.* 5 (1-2) (1995) 1–7, 5(1-2).
- [42] Y. Yang, C. Ochoa-Hernández, P. Pizarro, J.M. Coronado, D.P. Serrano, Effect of metal-support interaction on the selective hydrodeoxygenation of anisole to aromatics over Ni-based catalysts, *Appl. Catal. B: Env.* 145 (2014) 91–100.
- [43] K. Venkatachalam, P. Visuvamithiran, B. Sundaravell, M. Palanichamy, V. Murugesan, Catalytic performance of Al-MCM-48 molecular sieves for isopropylation of phenol with isopropyl acetate, *Chin. J. Catal.* 33 (2-3) (2012) 478–486.
- [44] D. Kubička, N. Kumar, T. Venäläinen, H. Karhu, I. Kubičková, H. Österholm, D. Yu. Murzin, Metal–support interactions in zeolite-supported noble metals: Influence of metal crystallites on the support acidity, *J. Phys. Chem. B* 110 (10) (2006) 4937–4946, 110(10).
- [45] A. Kayo, T. Yamaguchi, K. Tanabe, The effect of preparation method on the acidic and catalytic properties of iron oxide, *J. Catal.* 83 (1) (1983) 99–106.
- [46] A. Aho, N. Kumar, K. Eränen, T. Salmi, M. Hupa, D.Yu. Murzin, Catalytic pyrolysis of biomass in a fluidized bed reactor: influence of the acidity of H-beta zeolite, *Process Saf. Env. Prot.* 85 (5) (2007) 473–480.
- [47] I.L. Simakova, Z. Vajglová, M. Martínez-Klimov, K. Eränen, M. Peurla, P. Mäki-Arvela, D.Y. Murzin, One-pot synthesis of menthol from citral over Ni/H- $\beta$ -38 extrudates containing bentonite clay binder in batch and continuous reactors, *Org. Process Res. Dev.* 27 (2) (2023) 295–310.
- [48] E. Toukonit, P. Mäki-Arvela, N. Kumar, T. Salmi, D.Yu. Murzin, Continuous enantioselective hydrogenation of ethylbenzoylformate over Pt/Al<sub>2</sub>O<sub>3</sub> catalyst: bed dilution effects and cinchonidine adsorption study, *Catal. Lett.* 95 (2004) 179–183.
- [49] P. Mäki-Arvela, N. Kumar, V. Nieminen, R. Sjöholm, T. Salmi, D.Yu. Murzin, Cyclization of citronellal over zeolites and mesoporous materials for production of isopulegol, *J. Catal.* 225 (1) (2004) 155–169.
- [50] D.Y. Murzin, B. Kusema, E.V. Murzina, A. Aho, A. Tokarev, A.S. Boymirzaev, J. Wärnå, P.Y. Dapsens, C. Mondelli, J. Pérez-Ramírez, T. Salmi, Hemicellulose arabinogalactan hydrolytic hydrogenation over Ru-modified H-USY zeolites, *J. Catal.* 330 (2015) 93–105.

- [51] D. Pandey, G. Deo, Promotional effects in alumina and silica supported bimetallic Ni-Fe catalysts during CO<sub>2</sub> hydrogenation, *J. Mol. Catal. A: Chem.* 382 (2014) 23–30.
- [52] S.E.E. Misi, A. Ramli, Characterization of the structure feature of bimetallic Fe-Ni catalysts, *J. Appl. Sci.* 11 (2011) 1297–1302.
- [53] M. Nagai, O. Uchino, J. Okubo, S. Omi, TPR and XPS studies of iron-exchanged Y zeolites and their activity during dibenzothiophene hydrodesulfurization, *Stud. Surf. Sci. Catal.* 105 (1997) 989–995.
- [54] Q. Han, M.U. Rehman, J. Wang, A. Rykov, O.Y. Gutiérrez, Y. Zhao, S. Wang, X. Ma, J.A. Lercher, The synergistic effect between Ni sites and Ni-Fe alloy sites on hydrodeoxygenation of lignin-derived phenols, *Appl. Catal. B: Env* 253 (2019) 348–358.
- [55] A. Farooq, C.H. Ko, Y.K. Park, Sewage sludge steam gasification over bimetallic mesoporous Al-MCM48 catalysts for efficient hydrogen generation, *Env. Res.* 224 (2023) 115553.
- [56] Z. Vajglová, B. Gauli, P. Mäki-Arvela, N. Kumar, K. Eränen, J. Wärnå, R. Lassfolk, I. L. Simakova, I.P. Prosvirin, M. Peurla, J.K.M. Lindén, H. Huhtinen, P. Paturi, D. E. Doronkin, D.Yu Murzin, *ACS Appl. Nano Mat.* 6 (12) (2023) 10064–10077.
- [57] A. Puig-Molina, F.M. Cano, T.V.W. Janssens, The Cu promoter in an iron–chromium–oxide based water–gas shift catalyst under industrial conditions studied by in-Situ XAFS, *J. Phys. Chem. C* 114 (2010) 15410–15416.
- [58] S. Ali, Y. Abbas, Z. Zuhra, I.S. Butler, Synthesis of  $\gamma$ -alumina (Al<sub>2</sub>O<sub>3</sub>) nanoparticles and their potential for use as an adsorbent in the removal of methylene blue dye from industrial wastewater, *Nanoscale Adv.* 1 (1) (2019) 213–218.
- [59] Z. Vajglová, B. Gauli, P. Mäki-Arvela, I.L. Simakova, N. Kumar, K. Eränen, T. Tirri, R. Lassfolk, M. Peurla, D. Doronkin, D.Yu Murzin, Co-processing of fossil feedstock with lignin-derived model compound isoeugenol over Fe-Ni/HY-5.1 catalysts, *J. Catal.* 421 (2023) 101–116.
- [60] X.M. Zhu, M. Schön, U. Bartmann, A.C. Van Veen, M. Muhler, M. The dehydrogenation of ethylbenzene to styrene over a potassium-promoted iron oxide-based catalyst: a transient kinetic study, *Appl. Catal. A: Gen.* 266 (1) (2004) 99–108.
- [61] J. Cain, A. Laskin, M.R. Kholghy, M.J. Thomson, H. Wang, Molecular characterization of organic content of soot along the centerline of a coflow diffusion flame, *Phys. Chem. Chem. Phys.* 16 (2014) 25862–25875.
- [62] P. Yan, E. Kennedy, M. Stockenhuber, Hydrodeoxygenation of guaiacol over BEA supported bimetallic Ni-Fe catalysts with varied impregnation sequence, *J. Catal.* 404 (2021) 1–11.
- [63] E. Furimsky, E. Catalytic hydrodeoxygenation, *Appl. Catal. A: Gen.* 199 (2) (2000) 147–190, 199(2).
- [64] E.R. Sacia, M. Balakrishnan, M.A.T. Bell, Biomass conversion to diesel via the etherification of furanyl alcohols catalyzed by Amberlyst-15, *J. Catal.* 313 (2014) 70–79.
- [65] I. Nakamura, A. Zhang, K. Fujimoto, Selective synthesis of methylcyclopentane from cyclohexane using Pt-zeolite hybrid catalyst, *Stud. Surf. Sci. Catal.* 106 (1997) 561–566.
- [66] F.G. Gault, Mechanisms of skeletal isomerization of hydrocarbons on metals, *Adv. Catal.* 30 (1981) 1–95.
- [67] F. Ciapetta, Isomerization of saturated hydrocarbons, cycloalkanes, *Ind. Eng. Chem.* 45 (1) (1953) 159–162.
- [68] Y. Song, W. Lin, X. Guo, L. Dong, X. Mu, H. Tian, L. Wang, Aromatization and isomerization of methylcyclohexane over Ni catalysts supported on different supports, *Green. Energy Env* 4 (1) (2019) 75–82.